UC Berkeley
UC Berkeley Previously Published Works

Title

Dynamic stability of spinning viscoelastic cylinders at finite deformation

Permalink

https://escholarship.org/uc/item/59q6d7rb

Journal

International Journal of Solids and Structures, 51(21-22)

ISSN

0020-7683

Authors

Govindjee, Sanjay
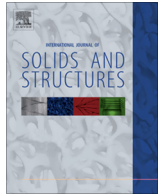Potter, Trevor
Wilkening, Jon

Publication Date

2014-10-01

DOI

10.1016/j.ijsolstr.2014.06.022

Peer reviewed

Dynamic stability of spinning viscoelastic cylinders at finite deformation

Sanjay Govindjee [a,*], Trevor Potter [b], Jon Wilkening [b]

[a] Department of Civil Engineering, University of California, Berkeley, Berkeley, CA 94720-1710, USA
[b] Department of Mathematics, University of California, Berkeley, Berkeley, CA 94720-3840, USA

ABSTRACT

The study of spinning axisymmetric cylinders undergoing finite deformation is a classic problem in several industrial settings – the tire industry in particular. We present a stability analysis of spinning elastic and viscoelastic cylinders using ARPACK to compute eigenvalues and eigenfunctions of finite element discretizations of the linearized evolution operator. We show that the eigenmodes correspond to N-peak standing or traveling waves for the linearized problem with an additional index describing the number of oscillations in the radial direction. We find a second hierarchy of bifurcations to standing waves where these eigenvalues cross zero, and confirm numerically the existence of finite-amplitude standing waves for the nonlinear problem on one of the new branches. In the viscoelastic case, this analysis permits us to study the validity of two popular models of finite viscoelasticity. We show that a commonly used finite deformation linear convolution model results in non-physical energy growth and finite-time blow-up when the system is perturbed in a linearly unstable direction and followed nonlinearly in time. On the other hand, Sidoroff-style viscoelastic models are seen to be linearly and nonlinearly stable, as is physically required.

© 2014 Elsevier Ltd. All rights reserved.

1. Introduction

The behavior of steady spinning bodies at finite deformation is of both theoretical and practical interest. In the special case that the body is axisymmetric, there has been a fair amount of work devoted to its formulation, elucidation, and behavior. Notable early work on the finite deformation spinning axisymmetric body is due to Padovan and Paramodilok (1983, 1985), Oden and Lin (1986), Padovan (1987), Bass (1987) and Kennedy and Padovan (1987). This literature formulates the equations of motion in the frame of reference of a non-spinning observer translating alongside the rotating body, and then to various degrees examines the equilibrium solutions of the motion as the spin rate is varied. The issues of contact with "roadways" and viscoelastic as well as elastic response are considered. The work of LeTallec and Rahier (1994), which followed this early work, provides the first clear description of the problem's kinematics and, by virtue thereof, lays the groundwork for the proper understanding of the issues associated with correctly specifying the constitutive response of a spinning body in a non-spinning frame of reference; see Govindjee and Mihalic (1998) for a discussion of this point, and the work of Faria et al.

(1992), which shows that the issue was somewhat understood prior to these latter two works.

A special feature of the response of a steady spinning elastic cylinder is the existence of non-axisymmetric stationary solutions (standing waves) that appear as bifurcations from an axisymmetric branch in the configuration space of the body (Oden and Lin, 1986; Chatterjee et al., 1999). The determination of these bifurcation speeds can be performed by searching for the spin rates at which the tangent operator of the equations of motion becomes singular. Similar non-axisymmetric steady spinning solutions have also been reported upon in the case of finite deformation viscoelasticity (Padovan and Paramodilok, 1983, 1985; Kennedy and Padovan, 1987; Chatterjee et al., 1999). However, in the viscoelastic case, external forcing through contact with a roadway or counter-rotating cylinder is required for these states to remain steady in time (Chatterjee et al., 1999).

In the present work, we study the linearized dynamics about the axisymmetric state of a freely spinning elastic or viscoelastic cylinder (not in contact with a roadway) and interpret all the eigenvalues and eigenfunctions as giving information on the dynamic behavior of the system on perturbation. We study the effect of rotating the eigenfunctions about the origin and classify them according to their rotational symmetry group and the number of radial oscillations in a tensor product representation. We are not aware that this structure of the eigenfunctions has previ-

* Corresponding author. Tel.: +1 510 642 6060.
  E-mail addresses: s_g@berkeley.edu (S. Govindjee), potter@math.berkeley.edu (T. Potter), wilkening@berkeley.edu (J. Wilkening).

ously been recognized. We also show that a typical eigenmode can be interpreted as a traveling wave that progresses around the cylinder in the lab frame with an angular velocity that depends on the imaginary part of the eigenvalue. In the elastic case, the real part of resolved eigenvalues (computed using ARPACK on a finite element discretization of the linearized evolution operator) is always found to be zero and the amplitude of the traveling wave remains constant in time. In the viscoelastic case, the wave decays (or grows) at a rate determined by the real part of the eigenvalue. In the special case of a zero eigenvalue, the traveling wave is actually stationary in time, indicating a potential bifurcation to a branch of finite-amplitude standing wave solutions. This is consistent with previous studies that predict such bifurcations when the tangent operator becomes singular.

The traveling wave description of the eigenmodes of the linearized problem provides a physical interpretation for the critical rotation speed ω_c beyond which bifurcations to standing wave solutions are possible. In the same way that a traveling water wave in a canal appears stationary to an observer riding alongside it on horseback (Russel, 1845), a traveling wave in a rotating elastic cylinder appears as a stationary solution in the lab frame if it travels backward through the medium at the speed of rotation. Below the critical speed, all modes of the linearized operator travel through the physical medium faster than the rotation rate, so a stationary solution is not possible. However, for special values of ω greater than ω_c, namely the values of ω where an eigenvalue of the tangent operator is zero, there is one wave traveling backward through the medium at the same rate that the medium travels forward. The fact that the bifurcation speeds ω accumulate at ω_c suggests that the traveling speed of a mode through the medium approaches a limiting value as the azimuthal wave number of the mode approaches infinity. In their monograph, Rabier and Oden (1989) offer a similar explanation in the incompressible case, crediting Faria with the insight, but using a half-plane analysis to predict wave speeds around the cylinder rather than interpreting eigenmodes as traveling waves.

In our framework, the traveling speeds of the eigenmodes are measured in the lab frame; thus, many highly complex spatial modes are found to travel slowly when $\omega > \omega_c$, since their speed through the medium is comparable to the speed of the medium in the opposite direction. This leads to an unusual and difficult eigenvalue problem in which the ordering of the eigenvalues along the imaginary axis has little correspondence with the spatial complexity of the modes. In light of these difficulties, it is remarkable that Rabier and Oden were able to prove existence of finite-amplitude standing wave branches in the incompressible case, with bifurcation points converging to ω_c from the right, using Lyapunov–Schmidt theory and Fredholm index theory.

Treating non-zero eigenvalues of the tangent operator on equal footing with the zero eigenvalues leads to many new questions. In particular, it is likely that families of finite-amplitude traveling solutions for the nonlinear problem bifurcate from non-zero (imaginary) eigenvalues. Computing such solutions would entail formulating the problem in a reference frame that rotates at the speed of the traveling wave in the lab frame, which is different than the rotation rate of the cylinder. Cyclic dynamics of the nonlinear problem may also result when bifurcations from superpositions of two linearized traveling waves exist. As a first step to exploring these possibilities, we show that one of the stationary modes that lies outside of the Oden and Lin hierarchy (due to a more complicated radial dependence) leads to a bifurcation branch of finite-amplitude solutions.

In the viscoelastic case, the eigenvalues have a non-zero real part, so rather than indicating bifurcations to pure stationary or traveling solutions, the eigenmodes also decay (or grow) in time at a rate determined by the magnitude (and sign) of the real part.

The imaginary parts of these eigenvalues behave much the same as in the elastic case, with a critical frequency ω_c beyond which many modes emerge with complex spatial structure that travel slowly or remain stationary in the lab frame; however, due to the non-zero real part of the eigenvalue, these modes decay (or grow) as they travel. Exponential growth of well-resolved eigenmodes indicates that the system is linearly unstable. When this occurs, we explore nonlinear stability by seeding the stationary solution with a perturbation in the unstable direction and evolving the system through time according to the full nonlinear evolution equations. Finite-time blow-up indicates a deficiency in the underlying (viscoelastic) material model.

An important issue when considering the mechanical response of continuum bodies is that the constitutive relations that are selected must satisfy the Clausius–Duhem inequality expressing the second law of thermodynamics; see e.g. Coleman and Noll (1963) or Truesdell and Noll (1965, Section 79). In the finite deformation viscoelastic setting there are two approaches to setting up such constitutive relations. One, due to Coleman (1964a,b), is to construct a free energy functional of the history of the material whose derivative with respect to the current deformation gradient yields a history functional giving the stress response. This framework seems natural for convolution type viscoelastic models, such as the well-known BKZ model (Bernstein et al., 1963) and the Simo model (Simo, 1987). Notwithstanding the popular status of these two models, and the formal appearance of convolution expressions in their specification, the requisite free-energy functional that generates them has never been reported. In other words, while these models have the appearance of being strictly dissipative, it is actually not known if they satisfy the Clausius–Duhem inequality except in the infinitesimal strain limit, where they do. An alternate viscoelastic framework is provided by the work of Sidoroff (1974), who proposes a multiplicative split of the deformation gradient, similar to finite deformation plasticity models, and then directly constructs evolution laws for the viscoelastic variables that satisfy the Clausius–Duhem inequality. Well known examples of models of this type are due to LeTallec and Rahier (1994) and Reese and Govindjee (1998b).

The spinning body problem provides an ideal setting for a deep comparison of these two distinctly different modeling frameworks. In particular we are able to demonstrate that models of the Simo-class become unstable (both linearly and nonlinearly) at high rotation rates, leading to non-physical results. By contrast, models of the Sidoroff-class behave well in similar situations. This point is particularly relevant for analysis schemes that rely upon a steady spinning state of a system followed by transient computation – e.g. in the modeling of a tire traveling at high speed that encounters a bump in the road.

An outline of the remainder of the paper is as follows: In Section 2 we review the strong and weak formulations of the elastic spinning body problem in both the steady and unsteady cases and discuss its Hamiltonian structure. In Section 3 we revisit the well-studied elastic bifurcation case to show that our formulation is consistent with previous work. We then go further to elucidate the structure of linearized solutions and identify a second hierarchy of bifurcations that have not been reported in numerical studies to our knowledge, but were mathematically foreshadowed in the monograph of Rabier and Oden (1989). We also compute a finite-amplitude standing wave on one of the new bifurcation branches. With this background, in Section 4 we present two viscoelastic models in a form suitable for the study of spinning bodies. This is followed in Section 5 by a stability analysis of the behavior of spinning viscoelastic cylinders and the strong influence of the choice of viscoelastic modeling framework. In Section 6 we consider a full nonlinear stability analysis and show that convolution-type viscoelastic models can lead to non-physical

instabilities at high rotation speeds that are not observed using either a purely elastic response or a Sidoroff-style viscoelastic model. The paper concludes with some brief comments and recommendations.

2. Elastic model

2.1. Domain and boundary conditions

The reference configuration $\mathcal{B}$ under consideration is an annulus centered at the origin with inner radius r_1 and outer radius r_2. Denoting material points $X = (X_1, X_2)$, we can write

$$\mathcal{B} = \{(X_1, X_2) \,|\, r_1 \leqslant \|X\|_2 \leqslant r_2\}. \tag{2.1}$$

We have inner boundary $\Gamma_h = \{X| \,\|X\|_2 = r_1\}$ called the hub and outer boundary $\Gamma_e = \{X| \,\|X\|_2 = r_2\}$ called the edge; see Fig. 1.

The hub is spun counter-clockwise about the origin at a constant angular velocity ω. If ϕ is the motion of the body, then we have the boundary condition

$$\phi(X, t) = \mathbf{R}(t)X \text{ on } \Gamma_h, \tag{2.2}$$

where $\mathbf{R}(t)$ is the rotation matrix given by

$$\mathbf{R}(t) = \begin{bmatrix} \cos(\omega t) & -\sin(\omega t) \\ \sin(\omega t) & \cos(\omega t) \end{bmatrix}. \tag{2.3}$$

On the edge, Γ_e, we prescribe traction-free boundary conditions.

2.2. Elastic constitutive equations

The motion is given by $\phi(X, t)$ with deformation gradient $\mathbf{F} = D\phi = \partial\phi/\partial X$. We assume a plane strain elastic response described by a compressible Mooney–Rivlin model, with stored energy function $\Psi_e(I_1, I_2, I_3)$. Ψ_e is given in terms of the invariants of the three dimensional right Cauchy–Green tensor

$$\mathbf{C}_3 = \begin{bmatrix} \mathbf{C} & 0 \\ 0 & 1 \end{bmatrix}, \tag{2.4}$$

where $\mathbf{C} = \mathbf{F}^\mathsf{T}\mathbf{F}$. We choose the stored energy function

$$\Psi_e = \frac{\kappa}{4}(I_3 - \log I_3 - 1) + \frac{\mu}{2}(1 - s)(I_1 - \log I_3 - 3)$$
$$+ \frac{\mu}{2}s(I_2 - 2\log I_3 - 3). \tag{2.5}$$

Here, $\kappa > 0$ is the bulk modulus, $\mu > 0$ is the shear modulus, and $s \in [0, 1]$ can be chosen to balance the two shear terms. This stored

Fig. 1. The reference domain $\mathcal{B}$.

energy function is noted to be polyconvex (Ciarlet, 1988, Section 4.9) and to satisfy the conditions for Ball's theory (Ball, 1977) of existence of solutions in finite deformation elasticity. From this expression, we can compute the first Piola–Kirchhoff stress tensor $\mathbf{P}_e$:

$$\mathbf{P}_e = \frac{\partial\Psi_e}{\partial\mathbf{F}} = \frac{\kappa}{2}(I_3 - 1)\mathbf{F}^{-T} + \mu(1 - s)(\mathbf{F} - \mathbf{F}^{-T}) + \mu s(I_1\mathbf{F} - \mathbf{F}\mathbf{C} - 2\mathbf{F}^{-T}). \tag{2.6}$$

2.3. Equations of motion

Given $\mathbf{P}_e$, the elastic equations of motion are formulated as

$$\rho_R\ddot{\phi} = \text{DIV } \mathbf{P}_e \text{ on } \mathcal{B} \tag{2.7}$$

with boundary conditions

$$\phi(X, t) = \mathbf{R}(t)X \text{ on } \Gamma_h, \\ \mathbf{P}_e\mathbf{N} = \mathbf{0} \text{ on } \Gamma_e. \tag{2.8}$$

ρ_R is the density of the undeformed material, which is assumed to be constant.

We reduce this second order equation in time to a system of first order equations in time by introducing the velocity of the motion, $\boldsymbol{v}(X, t)$, as an independent field variable. The equations of motion then become

$$\dot{\phi} = \boldsymbol{v} \text{ on } \mathcal{B}, \\ \dot{\boldsymbol{v}} = \frac{1}{\rho_R}\text{DIV } \mathbf{P}_e \text{ on } \mathcal{B} \tag{2.9}$$

with boundary conditions

$$\phi(X, t) = \mathbf{R}(t)X \text{ on } \Gamma_h, \\ \mathbf{P}_e\mathbf{N} = \mathbf{0} \text{ on } \Gamma_e. \tag{2.10}$$

If $(\phi, \boldsymbol{v})$ is a classical (as opposed to weak) solution, then $\boldsymbol{v}$ will also satisfy $\boldsymbol{v}(X, t) = \dot{\mathbf{R}}(t)X$ on Γ_h.

2.4. Steady spinning equations

We seek steady spinning states of the elastic body. Such a solution should satisfy

$$\phi(X, t) = \phi(\mathbf{R}(t)X, 0), \\ \boldsymbol{v}(X, t) = \boldsymbol{v}(\mathbf{R}(t)X, 0) \tag{2.11}$$

for all t. Following LeTallec and Rahier (1994), Oden and Lin (1986) and Govindjee and Mihalic (1998) among others, we introduce a new spatial variable $\widetilde{X}$ defined by

$$\widetilde{X} = \mathbf{R}(t)X. \tag{2.12}$$

We then define

$$\widetilde{\phi}(\widetilde{X}, t) = \phi(X, t), \\ \widetilde{\boldsymbol{v}}(\widetilde{X}, t) = \boldsymbol{v}(X, t). \tag{2.13}$$

Physically, we have decomposed the motion ϕ into a pure rotation $\mathbf{R}(t)$ followed by the deformation $\widetilde{\phi}$ that would be observed in the non-spinning "lab frame". Note that $\widetilde{\phi}$ assigns to a point the location of the material particle that would be there if the body were rotating rigidly with constant angular velocity. With this change of variables, the steady spinning conditions become

$$\widetilde{\phi}(\widetilde{X}, t) = \widetilde{\phi}(\widetilde{X}, 0), \\ \widetilde{\boldsymbol{v}}(\widetilde{X}, t) = \widetilde{\boldsymbol{v}}(\widetilde{X}, 0) \tag{2.14}$$

for all t. Thus the steady problem has been transformed into a problem that can be solved by setting $\dot{\widetilde{\phi}}$ and $\dot{\widetilde{\boldsymbol{v}}}$ equal to zero.
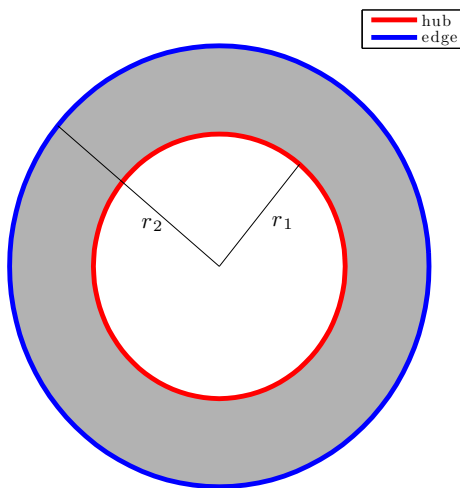
Returning to the full dynamics, we compute that $\widetilde{\phi}$ and $\widetilde{v}$ satisfy

$$\dot{\widetilde{\phi}} = \widetilde{v} - \mathbf{F}\Omega\widetilde{X},$$
$$\dot{\widetilde{v}} = \frac{1}{\rho_R}\widetilde{\mathrm{DIV}}\,\mathbf{P}_e - \widetilde{D}\widetilde{v}\Omega\widetilde{X}, \tag{2.15}$$

where $\widetilde{\mathbf{F}} \overset{\text{def}}{=} \widetilde{D}\widetilde{\phi}$, $\widetilde{\mathbf{C}} \overset{\text{def}}{=} \widetilde{\mathbf{F}}^{\mathsf{T}}\widetilde{\mathbf{F}}$, etc., and Ω is the constant matrix

$$\Omega = \dot{\mathbf{R}}\mathbf{R}^{\mathsf{T}} = \omega\begin{bmatrix} 0 & -1 \\ 1 & 0 \end{bmatrix}. \tag{2.16}$$

$\widetilde{D}$ and $\widetilde{\mathrm{DIV}}$ refer to derivatives with respect to $\widetilde{X}$. For ease of notation, we now drop the superposed tildes and refer to the transformed variables in what follows unless explicitly noted.

For later use, we also note the weak formulation of the equations of motion:

$$\int_{\mathcal{B}}\dot{\phi}\cdot\zeta = \int_{\mathcal{B}}(v - \mathbf{F}\Omega X)\cdot\zeta,$$
$$\int_{\mathcal{B}}\dot{v}\cdot\eta = \int_{\mathcal{B}} -\frac{1}{\rho_R}\mathbf{P}_e : D\eta + (D\eta)\Omega X\cdot v. \tag{2.17}$$

Here,

$$\phi - \boldsymbol{id} \in L^2([0,T], H_0^1(\mathcal{B})^2), \quad \zeta \in L^2(\mathcal{B})^2,$$
$$\dot{\phi},\; v \in L^2([0,T], L^2(\mathcal{B})^2), \qquad \eta \in H_0^1(\mathcal{B})^2,$$
$$\dot{v} \in L^2([0,T], H^{-1}(\mathcal{B})^2), \qquad \int_{\mathcal{B}}\dot{v}\cdot\eta \text{ means apply } \dot{v} \text{ to } \eta.$$

Also, the solution is defined for $0 < t < T$; spatial and temporal derivatives are interpreted weakly (Evans, 1998); $\boldsymbol{id}$ is the identity map on $\mathcal{B}$; L^2 refers to square-integrable functions; and $H^{-1}(\mathcal{B})$ is the dual space of $H_0^1(\mathcal{B})$, which is the Sobolev space of L^2 functions on $\mathcal{B}$ with a weak derivative in $L^2(\mathcal{B})$ and zero trace on the hub, Γ_h. We denote $\mathcal{G}(\phi, v)$ as the operator such that $(\dot{\phi}, \dot{v}) = \mathcal{G}(\phi, v)$, where $\dot{\phi}$, $\dot{v}$ satisfy (2.17). We remark that these spaces were chosen to be consistent with the theory of linear hyperbolic equations (Evans, 1998, Section 7.2). Less is known in the nonlinear elastodynamic case and additional spatial regularity is currently required to establish well-posedness; see Hughes et al. (1977) and the discussion in Marsden and Hughes (1983, Section 6.5).

As mentioned above, the steady spinning problem can now be written as

$$\mathbf{0} = v - \mathbf{F}\Omega X,$$
$$\mathbf{0} = \frac{1}{\rho_R}\,\mathrm{DIV}\,\mathbf{P}_e - Dv\Omega X \tag{2.18}$$

with boundary conditions

$$\phi(X,t) = X \text{ on } \Gamma_h,$$
$$\mathbf{P}_e\mathbf{N} = \mathbf{0} \text{ on } \Gamma_e. \tag{2.19}$$

For classical solutions, we also have $v(X,t) = \Omega X$ on Γ_h. In weak form the steady spinning problem can be written as

$$\mathcal{G}(\phi, v) = (\mathbf{0}, \mathbf{0}). \tag{2.20}$$

When convenient, we will denote the pair (ϕ, v) by $\mathbf{z}$. We may then write the steady state equations simply as $\mathcal{G}(\mathbf{z}) = \mathbf{0}$.

2.5. Hamiltonian structure

By virtue of our assumption of a stored energy function, the evolution of the untransformed variables is Hamiltonian, with Hamiltonian function

$$\int_{\mathcal{B}} \Psi_e + \frac{1}{2}\rho_R v\cdot v. \tag{2.21}$$

This is a non-autonomous system due to the time-dependent boundary conditions expressing rotation of the hub. However, the evolution of the transformed variables (2.17) is an autonomous Hamiltonian system described by the following Hamiltonian:

$$\mathcal{H} = \int_{\mathcal{B}} \Psi_e + \frac{1}{2}\rho_R v\cdot v - \rho_R(\mathbf{F}\Omega X)\cdot v. \tag{2.22}$$

Below we will discretize the equations and obtain a finite dimensional Hamiltonian system to which we can apply stability theory. In particular, let $\hat{\mathcal{H}}$ be the discretized Hamiltonian and let $\hat{\mathcal{G}}$ be the discretization of $\mathcal{G}$, which describes the motion generated by $\hat{\mathcal{H}}$: $\rho_R\hat{\mathcal{G}} = (\partial\hat{\mathcal{H}}/\partial v, -\partial\hat{\mathcal{H}}/\partial\phi)$. It will be useful to note that the Hessian of $\hat{\mathcal{H}}$ is related to the Jacobian of $\hat{\mathcal{G}}$ by $\rho_R D\hat{\mathcal{G}} = \mathcal{J}D^2\hat{\mathcal{H}}$, where $\mathcal{J} = \begin{bmatrix} \mathbf{0} & \mathbf{I} \\ -\mathbf{I} & \mathbf{0} \end{bmatrix}$ is skew-symmetric. Later we will use the following theorem about the stability of Hamiltonian systems: If $\mathbf{z}_0$ is a critical point of $\hat{\mathcal{H}}$ and the matrix $D^2\hat{\mathcal{H}}$ is positive definite at $\mathbf{z}_0$, then $\mathbf{z}_0$ is Lyapunov stable, since energy level sets near $\hat{\mathcal{H}}(\mathbf{z}_0)$ remain close to $\mathbf{z}_0$. In turn, Lyapunov stability implies that the eigenvalues of $D\hat{\mathcal{G}}$ are purely imaginary, since otherwise $\mathbf{z}_0$ would be linearly unstable either forward or backward in time. Indeed, if $\hat{\mathcal{G}}(\mathbf{z}_0) = 0$ and $D\hat{\mathcal{G}}[\mathbf{z}_0]\mathbf{z}_1 = \lambda\mathbf{z}_1$, where $\lambda = \gamma + \mathrm{i}\beta$ with $\gamma,\ \beta$ real, then

$$\mathbf{z} = \mathbf{z}_0 + \mathrm{Re}\{\varepsilon e^{\lambda t}\mathbf{z}_1\} = \mathbf{z}_0 + \varepsilon e^{\gamma t}(\mathrm{Re}\{\mathbf{z}_1\}\cos\beta t - \mathrm{Im}\{\mathbf{z}_1\}\sin\beta t) \tag{2.23}$$

satisfies $\dot{\mathbf{z}} = \hat{\mathcal{G}}(\mathbf{z}) + O(\varepsilon^2)$; note that $\mathrm{i} = \sqrt{-1}$ is the imaginary unit. Clearly, $\bar{\lambda} = \gamma - \mathrm{i}\beta$ is also an eigenvalue. If $\mathbf{z}_0$ has the additional symmetry that time-reversal is equivalent to spatial reflection about the y-axis (or any other axis passing through the origin), then $-\lambda$ and $-\bar{\lambda}$ will also be eigenvalues, though not necessarily distinct from $\bar{\lambda}$ and λ. In this case, linear stability or instability forward in time implies the same backward in time, and vice versa. Every stationary solution we know of possesses this additional symmetry.

3. Perturbations of the elastic model

Oden and Lin (1986) numerically solved the steady state problem (2.20) in an equivalent form. Below a certain critical speed ω_c, they only observed an axisymmetric solution. However, for some $\omega \geq \omega_c$, they found bifurcations to non-axisymmetric solutions by noticing that the Jacobian matrix $D\mathcal{G}$ of $\mathcal{G}$ about an axisymmetric solution $\mathbf{z}$ becomes singular. We repeat this analysis but, in addition to the 0 eigenvalues studied by Oden and Lin, we also track a set of small-magnitude eigenvalues of $D\mathcal{G}$. As discussed above, this gives information about the behavior of the system under dynamic perturbation. In the remainder of this section, we first describe the numerical methods we employ and then describe the results of our experiments.

3.1. Numerical methods

We employ quartic quadrilateral C^0 isogeometric elements to discretize the weak equations, which in turn allows us to compute $\hat{\mathcal{G}}$, the discretization of $\mathcal{G}$ (see Fig. 2). Although the weak formulation for the continuous problem calls for $\phi(t) - \boldsymbol{id} \in H_0^1(\mathcal{B})^2$ and $v(t) \in L^2(\mathcal{B})^2$ to live in different spaces, we use the same finite element basis functions to represent ϕ and v, which is necessary in a method of lines discretization. In addition to $\phi(X,t) = X$ on Γ_h, we impose the redundant boundary condition $v(X,t) = \Omega X$ on Γ_h and use test functions $\zeta,\ \eta$ that are zero on Γ_h. This yields square, symmetric mass matrices when solving for $\dot{\phi}$, $\dot{v}$ in (2.17). We do not encounter any numerical difficulties imposing redundant boundary conditions on v, and in fact this is common practice to improve condition numbers in first-order least-squares finite elements (Cai et al., 1997a,b). The advective terms $\mathbf{F}\Omega X$ and $Dv\Omega X$ do not cause numerical difficulty either, so we did not find it necessary to experiment

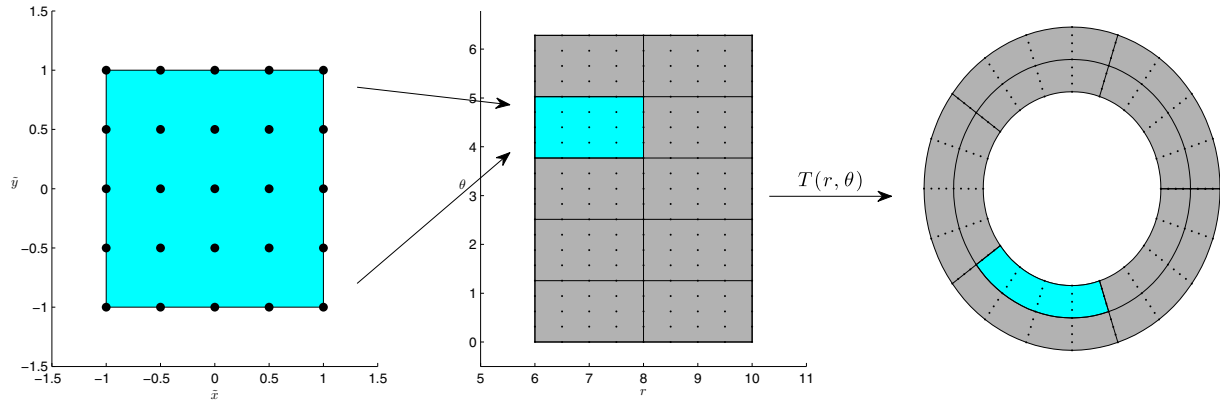**Fig. 2.** The reference element is mapped to the r–θ plane, where it is then mapped by the polar coordinate transformation exactly onto the annular reference configuration $\mathcal{B}$.

with upwind schemes; this is perhaps helped by the fact that by discretizing the r–θ plane, our finite element discretization of $\mathbf{F}\Omega$ exactly respects the (streamline) trajectories.

By linearizing the weak equations about a given $\mathbf{z} = (\boldsymbol{\phi}, \mathbf{v})$, we can also compute the Jacobian matrix $D\hat{\mathcal{G}}$. When we wish to emphasize the function about which $\hat{\mathcal{G}}$ is linearized, we will write $D\hat{\mathcal{G}}[\mathbf{z}]$. We note that $D\hat{\mathcal{G}}$ can be written as the product $\mathcal{M}^{-1}\mathcal{A}$, where $\mathcal{M}$ is the mass matrix corresponding to the finite element basis. Both $\mathcal{M}$ and $\mathcal{A}$ are sparse due to the finite element formulation. We solve the steady-state Eq. (2.20) using Newton's method. We must perform matrix solves on $D\hat{\mathcal{G}}$, hence $\mathcal{A}$, for which we employ the direct sparse solver SuperLU (Li and Demmel, 2003).

To compute eigenvalues of $D\hat{\mathcal{G}}$, we employ the Arnoldi method implemented in the ARPACK software package (Lehoucq et al., 1998). This method works best finding large magnitude eigenvalues, so in order to find small-magnitude eigenvalues we apply it to $(D\hat{\mathcal{G}})^{-1}$. Exactly as with Newton's method, we perform matrix solves on $D\hat{\mathcal{G}}$ using SuperLU.

3.2. Results: classic modes

We first state our choice of units and choice of constants. Our units are Newtons (N), megagrams (Mg), and seconds (s). This choice implies our unit for length is millimeters (mm). Our body has inner radius $r_1 = 240$ mm and outer radius $r_2 = 400$ mm. The density of the body is $\rho = 10^{-9}$ Mg/mm³. The bulk modulus κ and shear modulus μ are 689 N/mm² and 6.89 N/mm², respectively, and we set $s = 0.5$ in the stored energy function (2.5).

We briefly recall the results of Oden and Lin in some detail. For any rotation speed ω, they found an axisymmetric solution $\mathbf{z}_\omega$. For small ω they observed that $D\hat{\mathcal{G}}[\mathbf{z}_\omega]$ is non-singular, but at a speed ω_c they found that $D\hat{\mathcal{G}}[\mathbf{z}_\omega]$ became highly singular, i.e. $D\hat{\mathcal{G}}[\mathbf{z}_\omega]$ had a large dimensional nullspace. For $\omega > \omega_c$, they observed discrete speeds ω_i, $3 \leqslant i < \infty$, where $D\hat{\mathcal{G}}[\mathbf{z}_{\omega_i}]$ also became singular. Perturbing away from the axisymmetric solution in the direction of a null vector of $D\hat{\mathcal{G}}[\mathbf{z}_{\omega_i}]$ led to an i-peak standing wave solution to the steady spinning problem. They noted that the ω_i decrease monotonically and limit to ω_c from above. Thus Oden and Lin discovered a hierarchy of i-peak standing wave solutions.

Using ARPACK, in addition to nullspaces, we compute the smallest eigenvalues of the matrix $D\hat{\mathcal{G}}[\mathbf{z}_\omega]$ for a range of values of ω and plot them in Fig. 3. This gives information on dynamic stability in addition to identifying potential bifurcations to standing-wave solutions. When $\omega < \omega_c$, the eigenvalues are all purely imaginary. This is explained by the Hamiltonian structure of the problem. When $\omega = 0$, the axisymmetric solution is the identity configuration and we can directly compute that $D^2\hat{\mathcal{H}}$ is positive definite. As we increase ω to ω_c, we numerically observe that $D^2\hat{\mathcal{H}}$ remains
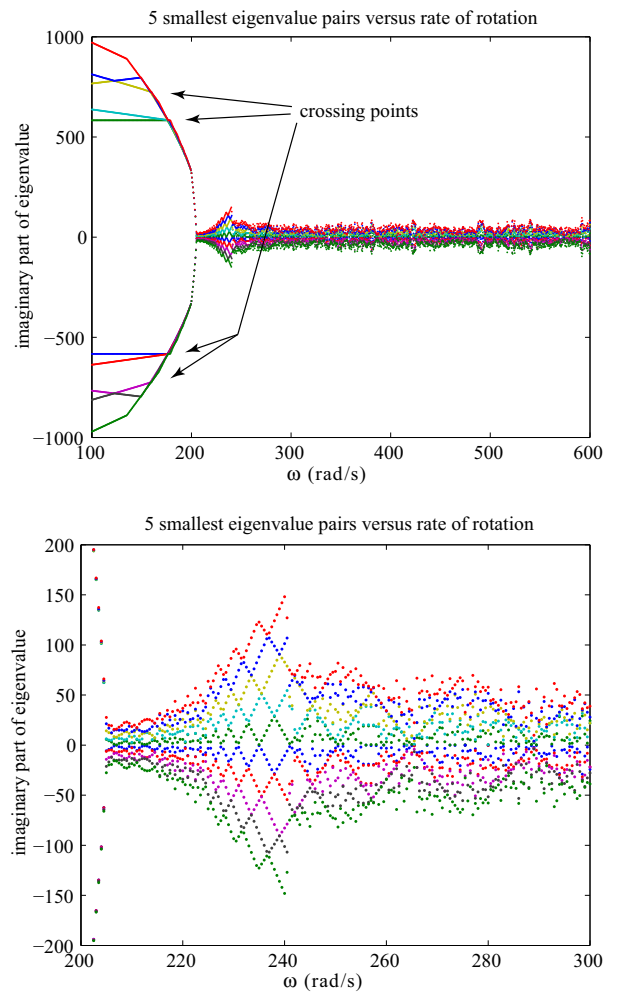

Fig. 3. Plots of the smallest eigenvalues of $D\hat{\mathcal{G}}[\mathbf{z}_\omega]$. Here ω_c is near 210 rad/s and a mesh with 8 radial elements and 64 angular elements has been used. The marked crossing points indicate where eigenvalues initially outside the axis range enter the set of the smallest eigenvalues – resulting in an *only apparently* non-smooth structure.

positive definite. Thus, the Hamiltonian serves as a Lyapunov function to ensure nonlinear (and hence linear) stability, which our eigenvalue computations confirm. For $\omega > \omega_c$, the Hessian may lose positive definiteness, and we can no longer use the Hamiltonian as a Lyapunov function. However, as explained below, all

resolved eigenvalues continue to be purely imaginary in our numerical studies, so that the system remains linearly stable for all values of $\omega > \omega_c$ that we computed. This is consistent with the findings of Rabier and Oden (1989) in the incompressible case, who concluded that bifurcation to non-trivial steady-state solutions could not be attributed to loss of stability of the trivial branch since the trivial branch remains stable up to $\omega = \sqrt{3}$, which exceeds $\omega_c = 0.9553$ (in dimensionless units).

In the top plot of Fig. 3, we see that the smallest eigenvalues are bounded away from 0 initially and then rapidly move toward 0 through a sequence of crossing events described below. Where they collide with 0 indicates that $D\hat{\mathcal{G}}[\mathbf{z}_\omega]$ has lost rank and identifies ω_c. The lower plot of Fig. 3 is a zoomed-in portion of the upper plot. There we can see a series of Xs that accumulate at $\omega_c \approx 210$ rad/s when approached from the right. These Xs cross zero at the bifurcation speeds ω_i where $D\hat{\mathcal{G}}[\mathbf{z}_\omega]$ is singular, indicating a candidate location for a branch of i-peak standing wave solutions to meet the trivial (i.e. axisymmetric) branch.

A consequence of plotting only the 5 smallest eigenvalues is that slowly-varying eigenvalues disappear from the plot when rapidly varying eigenvalues cross them. Some of these crossing points are labeled in the top plot of Fig. 3. The curves coming in from the left actually persist along their slowly varying trajectories (without sharply changing slope), but they cease to be among the "smallest five" after the crossing event. At low rotation speeds, smaller eigenvalues correspond to simpler eigenfunctions. However, as ω increases, large eigenvalues with highly complex eigenfunctions decrease rapidly and cross the real axis shortly after ω_c. The eigenvalues with simpler eigenfunctions cross the real axis later. Physically, crossing ω_c leads to many spatially complex waves (for the linearized problem) that oscillate slowly in time. Mixed in with these are spatially simple modes that can be resolved accurately by the finite element mesh.

The sporadic eigenvalues in Fig. 3 not lying on an X were never found to correspond to resolved eigenfunctions and do not persist when the mesh is refined. Occasionally these (sporadic) eigenvalues will have a non-zero real component, but we did not observe any of these in which the corresponding eigenfunction was well-resolved. In the incompressible case, Rabier and Oden (1989) proved that the eigenvalues are purely imaginary for rotation speeds well beyond ω_c. We conjecture that the same is true here, i.e. the non-zero real components we obtain in some of the eigenvalues are due to the discretization of the equations. If we plot only the eigenvalues that correspond to the ω_i, $i = 2, \ldots, 12$, we obtain Fig. 4. We will denote these eigenvalues as $\lambda_i(\omega)$ with complex conjugate $\bar{\lambda}_i(\omega)$. Note that $\lambda_i(\omega_i) = 0$. For each λ_i and $\bar{\lambda}_i$ there is a complex conjugate pair of eigenfunctions that combine

to give the oscillatory modes $\mathrm{Re}\{\mathbf{z}_1\}$ and $\mathrm{Im}\{\mathbf{z}_1\}$ in (2.23). We will denote the eigenfunction associated with λ_i by $\mathbf{e}_i(\omega)$. The real ϕ components of two of the $\mathbf{e}_i$ are plotted in Fig. 5.

3.3. Results: radial hierarchy

In addition to the standing wave eigenfunctions with i peaks we discovered other eigenfunctions which correspond to other bifurcation speeds. We plot these eigenfunctions in Fig. 6 and note that these eigenfunctions have more complexity in the radial direction than the eigenfunctions discussed by Oden and Lin. To investigate this, we note that the rotational symmetry of our problem implies that eigenfunctions must have a certain form. $D\mathcal{G}$ commutes with a family of rotation operators $\mathcal{R}(\alpha)$ defined by

$$\mathcal{R}(\alpha)\begin{pmatrix}\bar{\phi}\\\bar{v}\end{pmatrix}(X) = \begin{pmatrix}\mathbf{R}(\alpha)\bar{\phi}(\mathbf{R}^\mathsf{T}(\alpha)X)\\\mathbf{R}(\alpha)\bar{v}(\mathbf{R}^\mathsf{T}(\alpha)X)\end{pmatrix}, \tag{3.1}$$

where $\mathbf{R}(\alpha)$ is the rotation matrix of (2.3) with ωt replaced by α and a bar denotes a vector in the tangent space. Hence, any eigenfunction $\bar{\mathbf{z}} = (\bar{\phi}, \bar{v})$ of $D\mathcal{G}$ associated to a distinct eigenvalue must also be an eigenfunction of $\mathcal{R}(\alpha)$ for all α. This implies, as shown below, that $\bar{\mathbf{z}} = (\bar{\phi}, \bar{v})$, written as a function of polar coordinates, is of the form

$$\begin{aligned}\bar{\phi}(r,\theta) &= a_1(r)e^{-\mathrm{i}(k+1)\theta}\begin{bmatrix}1\\\mathrm{i}\end{bmatrix} + a_2(r)e^{-\mathrm{i}(k-1)\theta}\begin{bmatrix}1\\-\mathrm{i}\end{bmatrix},\\\bar{v}(r,\theta) &= a_3(r)e^{-\mathrm{i}(k+1)\theta}\begin{bmatrix}1\\\mathrm{i}\end{bmatrix} + a_4(r)e^{-\mathrm{i}(k-1)\theta}\begin{bmatrix}1\\-\mathrm{i}\end{bmatrix}\end{aligned} \tag{3.2}$$

and $\mathcal{R}(\alpha)\bar{\mathbf{z}} = e^{\mathrm{i}k\alpha}\bar{\mathbf{z}}$. Here, k is a fixed integer and the $a_i(r)$ are functions that depend only on the radial coordinate r. Writing $\lambda = \gamma + \mathrm{i}\beta$ as in (2.23), perturbation of the initial condition by $\mathrm{Re}\{\varepsilon\bar{\mathbf{z}}\}$ evolves as $\bar{\zeta}(t) = \mathrm{Re}\{\varepsilon e^{\gamma t}e^{\mathrm{i}\beta t}\bar{\mathbf{z}}\}$ under the linearized dynamics. If $k = 0$, this linearized solution remains axisymmetric for all time (since $\mathcal{R}(\alpha)\bar{\zeta} = \bar{\zeta}$ for all α), but pulsates (if $\beta \neq 0$) and grows or decays (if $\gamma \neq 0$). Otherwise,

$$\bar{\zeta}(t) = e^{\gamma t}\mathcal{R}\left(\frac{2\pi n + \beta t}{k}\right)\mathrm{Re}\{\varepsilon\bar{\mathbf{z}}\}, \quad (n \in \mathbb{Z}), \tag{3.3}$$

i.e. this mode is invariant when rotated by $2\pi n/|k|$ and travels around the cylinder with angular velocity β/k and decay rate γ. As discussed above, γ has always been found to be zero in the elastic case for resolved eigenfunctions in our numerical studies. Note that bifurcation to a standing wave with N peaks corresponds to an eigenvalue $\lambda = 0$ (so the wave does not travel or decay) with eigenfunction of the form (3.2) with $k = N$ or $k = -N$.
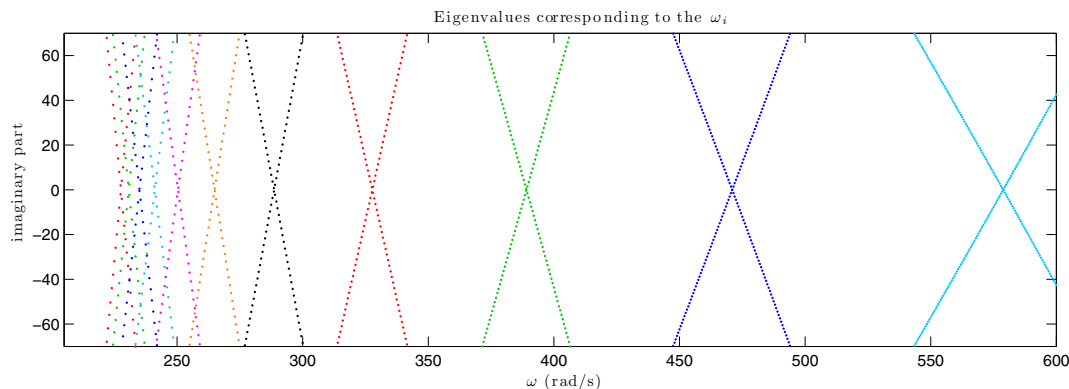

Fig. 4. Plot of the λ_i and $\bar{\lambda}_i$. The leftmost X corresponds to λ_{12} while the rightmost X corresponds to λ_2.

Eigenvector corresponding to ω_{12} Eigenvector corresponding to ω_5
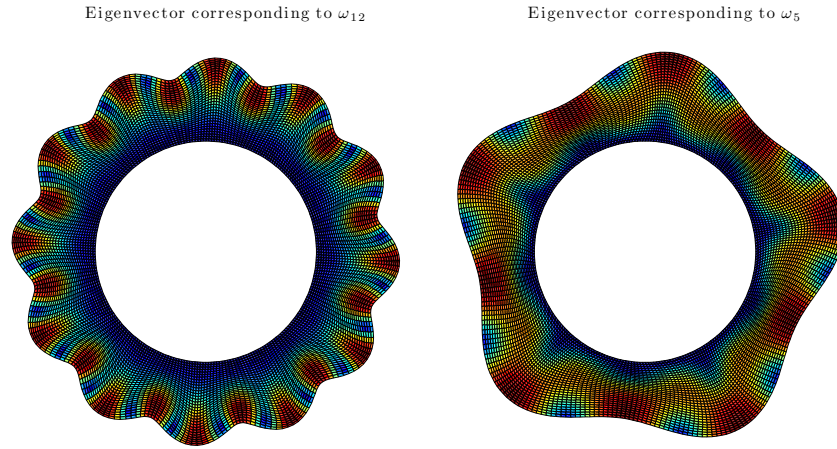

Fig. 5. Plot of the real ϕ component of $\mathbf{e}_{12}$ and $\mathbf{e}_5$. The plots are colored according to the norm of the real ϕ component, with red being large and blue small. (For interpretation of the references to color in this figure legend, the reader is referred to the web version of this article.)
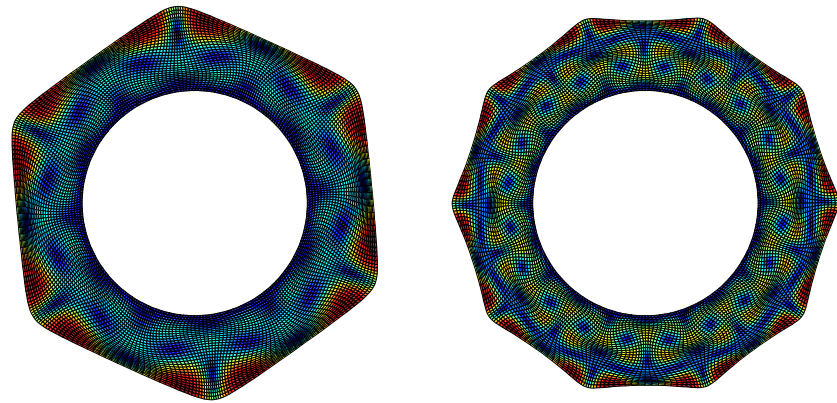

Fig. 6. Plot of the real ϕ component of eigenfunctions outside of the N-peak hierachy discovered by Oden and Lin. The plots are colored according to the displacement from the reference configuration, with red being high displacement and blue being little displacement. (For interpretation of the references to color in this figure legend, the reader is referred to the web version of this article.)

An interesting question that has not, to our knowledge, been explored concerns existence of families of finite-amplitude traveling waves, or of more exotic traveling-breathing solutions of the nonlinear equations. Pure traveling waves are only a minor generalization of standing waves as they only require a reformulation of the equations in a reference frame that rotates at the speed of the traveling wave rather than remaining fixed in the lab or rotating at the same speed as the body. However, proving existence or computing cyclic breathing solutions that bifurcate from a superposition of linearized traveling waves would likely be difficult, perhaps comparable to studying time-periodic water waves (Iooss et al., 2005; Wilkening, 2011; Wilkening and Yu, 2012; Rycroft and Wilkening, 2013). Standing waves in a rotating cylinder are observed in laboratory experiments (e.g. Chatterjee et al., 1999) because contact is required to overcome energy dissipation ($\gamma < 0$) due to viscoelasticity, and the contact region remains stationary in the lab frame, precluding waves that travel.

To see that the form in (3.2) must hold, we first consider the eigenfunction equation for $\bar{\phi}$ with undetermined eigenvalue $\lambda(\alpha)$:

$$\mathbf{R}(\alpha)\bar{\phi}(\mathbf{R}^\mathsf{T}(\alpha)X) = \lambda(\alpha)\bar{\phi}(X).$$

In polar coordinates this becomes

$$\mathbf{R}(\alpha)\bar{\phi}(r, \theta - \alpha) = \lambda(\alpha)\bar{\phi}(r, \theta). \tag{3.4}$$

Decomposing $\bar{\phi}$ into the Fourier series $\bar{\phi}(r, \theta) = \sum_{-\infty}^{\infty} \mathbf{c}_n(r)e^{in\theta}$ and matching terms yields

$$\mathbf{R}(\alpha)\mathbf{c}_n(r) = \lambda(\alpha)e^{in\alpha}\mathbf{c}_n(r) \quad \text{for all } n.$$

As the only eigenvalues of $\mathbf{R}(\alpha)$ are $e^{\pm i\alpha}$, either $\mathbf{c}_n(r) = \mathbf{0}$ or

$$\mathbf{c}_n(r) = c_n(r)\begin{bmatrix} 1 \\ i \end{bmatrix}, \quad \lambda(\alpha)e^{in\alpha} = e^{-i\alpha} \tag{3.5}$$

or

$$\mathbf{c}_n(r) = c_n(r)\begin{bmatrix} 1 \\ -i \end{bmatrix}, \quad \lambda(\alpha)e^{in\alpha} = e^{i\alpha}. \tag{3.6}$$

Since $\bar{\phi}$ is not identically zero, (3.5) or (3.6) holds for at least one n. Since $\lambda(\alpha)$ is independent of n, there is a k for which $\lambda(\alpha) = e^{ik\alpha}$, and all $\mathbf{c}_n$ must be zero except for $n = -k - 1$, with $\mathbf{c}_n$ of the form (3.5), and $n = -k + 1$, with $\mathbf{c}_n$ of the form (3.6). The same argument applies to $\bar{v}$.

Given a numerically computed eigenfunction with N peaks, we can compute its Fourier series in the θ direction. As expected due to (3.2), we observe exactly two Fourier modes: $N \pm 1$ or $-N \pm 1$. We repeat this computation for each value of r (65 values in our numerical simulations) to determine the functions $a_i(r)$ in (3.2). By plotting the a_i we can compare the radial complexity of different eigenfunctions. As in the upper left plot in Fig. 7, we observe the $a_i(r)$ corresponding to the $\mathbf{e}_i$ have one local extremum. The $a_i(r)$ corresponding to other eigenfunctions have more radial complexity with 2, 3, 4 or more local extrema.
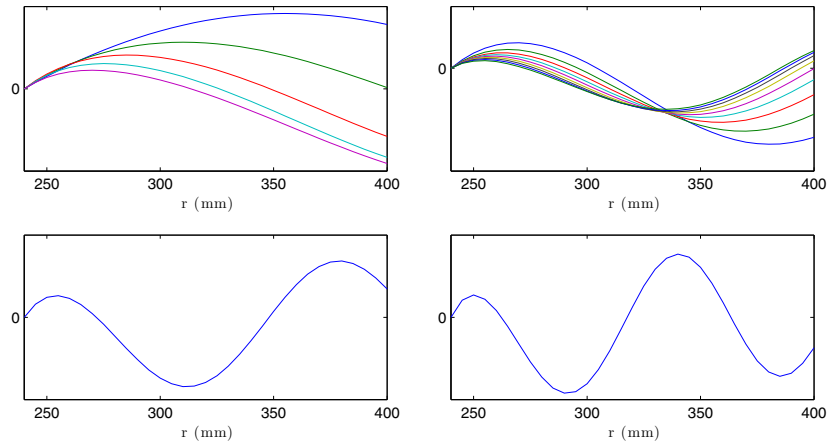
Fig. 7. Plots of the real part of a_1 for various eigenfunctions. The top left plot corresponds to the $\mathbf{e}_i$. The top right plot corresponds to *N*-peak bifurcations with extra radial complexity. The bottom plots correspond to eigenfunctions with even greater radial complexity.

Examining these solutions, we find an entire *N*-peak hierarchy of eigenfunctions with a_i having two local extrema. We denote these eigenfunctions by $\mathbf{e}_{i,2}$ with corresponding eigenvalues and bifurcation speeds denoted $\lambda_{i,2}$ and $\omega_{i,2}$, respectively. Fig. 8 shows the corresponding paths of their eigenvalues. As in Figs. 6 and 7, we also found eigenvalues with more radial complexity than the $\mathbf{e}_{i,2}$, which suggests that standing wave solutions may be described by a two-dimensional hierarchy $\mathbf{e}_{i,j}$, where *i* is the number of peaks in the circumferential direction and *j* is the number of oscillations in the radial direction. We do not have enough numerical data to determine whether the $\omega_{i,j}$ converge to ω_c as $i \rightarrow \infty$ for fixed *j*, or if perhaps there is a distinct critical speed for each *j*. However, the physical interpretation of ω_c as the limiting wave speed of high azimuthal wave-number modes propagating backward through the medium as it spins suggests that the critical speed ω_c is independent of *j*. We do not know if there could be multiple limiting wave speeds corresponding to shear waves and compression waves.

In their monograph, Rabier and Oden (1989) discovered analytically a two-dimensional hierarchy of eigenvalues $\zeta_{i,j}$ of an operator related to $D\mathcal{G}$. However, their analysis was not able to show that the $\zeta_{i,j}$ correspond to eigenvalues of $D\mathcal{G}$ for $j > 1$, and it applies only to incompressible hyperelastic materials. Incompressibility enables the use of potential functions to describe the solutions on other branches, but prevents solutions on the trivial branch of stationary solutions from expanding radially. One of their results is that the linearization of the operator they use to study bifurcation to nontrivial stationary solutions fails to be Fredholm at precisely one value of the dimensionless rotation speed in the range $0 < \omega < 1$, namely at $\omega_c = 0.9553$. This gives further support, at

least in the incompressible case when only shear waves are present, for the conjecture that each sequence $\omega_{i,j}$ converges to the same ω_c as $i \rightarrow \infty$ rather than having a distinct critical speed for each *j*.

We conclude this section with numerical evidence that the eigenfunctions $\mathbf{e}_{i,j}$ with $j \geq 2$ yield bifurcations to actual branches of nonlinear finite-amplitude standing wave solutions. For this purpose, we arbitrarily select the $i = 6$ peak eigenfunction in the second level of the hierarchy (left plot of Fig. 6) and search for a stationary solution of the nonlinear problem using a perturbation in the $\mathbf{e}_{6,2}$ direction as a starting guess. The finite element mesh has 33 grid points in the radial direction and 256 grid points in the azimuthal direction. The amplitude is constrained by requiring that the dot product in $\mathbb{R}^{33 \times 256}$ with $\text{Re}\{\mathbf{e}_{6,2}\}$ is equal to 1.0 (selected arbitrarily). Newton's method was used to rapidly converge to the solution of the nonlinear equations using SuperLU for the sparse matrix factorizations of the linearized operators that arise. The results, plotted in Fig. 9, show that the finite-amplitude standing wave has a similar internal structure to the perturbation direction $\mathbf{e}_{6,2}$ of Fig. 6, as expected.

4. Viscoelastic effects

In Section 3, we presented a linear stability analysis of a spinning elastic cylinder along with a discussion of an additional hierarchy of bifurcation modes not reported on to date. In this section, we consider the influence of viscoelasticity on the stability of a spinning cylinder and, in particular, we discuss the influence of the choice of the (finite deformation) viscoelastic model. More specifically, viscoelasticity causes the eigenvalues to acquire a real
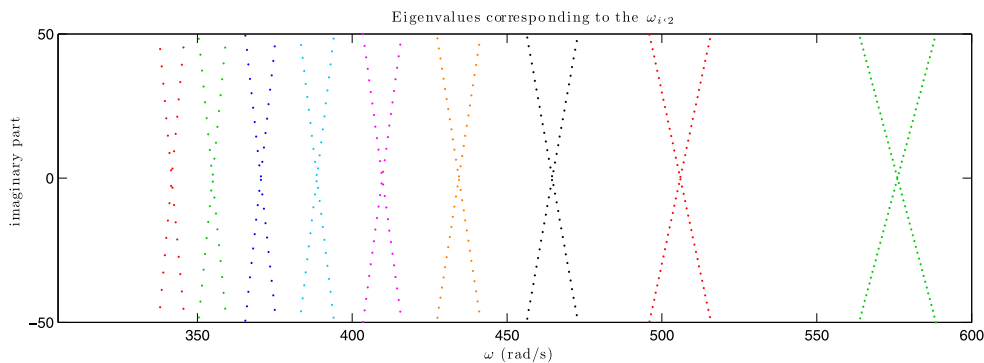

Fig. 8. Plot of the $\lambda_{i,2}$ and $\bar{\lambda}_{i,2}$. The leftmost X corresponds to $\lambda_{12,2}$ while the rightmost X corresponds to $\lambda_{4,2}$.
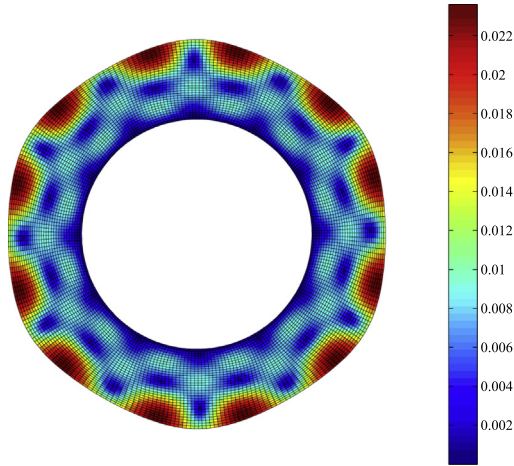
Fig. 9. Finite-amplitude standing-wave solution of the nonlinear elastic equations with 6 peaks that lies outside of the Oden–Lin hierarchy of bifurcations (due to $j = 2$). The contour plot shows the magnitude of the deviation in displacement from the axisymmetric solution where the bifurcation occurred. The displacements were amplified by a factor of 500 when plotting the mesh to better visualize the state of deformation.

part γ, which normally causes exponential decay in (3.3) when the stationary solution is perturbed in the direction of an eigenfunction. However, in the finite deformation linear viscoelastic model proposed by Simo (1987), γ can be positive, indicating an unstable mode. Evolving this mode beyond the linearized regime leads to non-physical blow-up, indicating that the mechanism in the model for dissipating energy can actually add energy to the system. By contrast, a nonlinear Sidoroff-style (Sidoroff, 1974) model detailed by Govindjee and Reese (1997) and Reese and Govindjee (1998a,b) always yields stable linear perturbations ($\gamma < 0$), and we do not observe instabilities when evolving the full (as opposed to linearized) equations either.

In both the linear and nonlinear models, additional variables are introduced that govern a viscoelastic component of the first Piola–Kirchhoff stress tensor, which we denote $\mathbf{P}_v$. The equations of motion are then driven by the total Piola–Kirchhoff stress tensor $\mathbf{P}_{total} = \mathbf{P}_e + \mathbf{P}_v$. We briefly describe the two models below. For the purpose of describing the models in a general context, we will revert to using ϕ, v, $\mathbf{F}$, etc. as the untransformed variables and $\widetilde{\phi}$, $\widetilde{v}$, $\widetilde{\mathbf{F}}$, etc. as the transformed variables.

4.1. Finite deformation linear viscoelastic model

We refer to the model of Simo (1987) as a (finite deformation) linear model because the evolution of the viscoelastic variables can be described by a differential equation that is linear in the viscoelastic variables – even though it was designed to be applied to finite deformation problems.

The model is often presented by first introducing a viscoelastic over-stress tensor $\mathbf{Q}$ defined by the convolution equation

$$\mathbf{Q}(t) = \int_{-\infty}^{t} \exp\left(\frac{-(t-s)}{\tau}\right) \frac{d}{ds}(\mathbf{S}_e(s))\, dt. \tag{4.1}$$

Here $\mathbf{S}_e = \mathbf{F}^{-1}\mathbf{P}_e$ is the second Piola–Kirchhoff stress tensor corresponding to $\mathbf{P}_e$ and τ is the viscoelastic relaxation time. Differentiating (4.1) yields an evolution equation for $\mathbf{Q}$:

$$\dot{\mathbf{Q}}(t) = -\frac{1}{\tau}\mathbf{Q}(t) + \dot{\mathbf{S}}_e(t). \tag{4.2}$$

Quiescent initial conditions correspond to setting $\mathbf{Q}(0) = \mathbf{0}$. Note that the evolution depends linearly on $\mathbf{Q}$. Given $\mathbf{Q}$, we define a vis-

coelastic second Piola–Kirchhoff stress tensor $\mathbf{S}_v$ by $\mathbf{S}_v = v\mathbf{Q}$, where v is a weight parameter describing the strength of the viscoelastic response. We then define $\mathbf{P}_v = \mathbf{F}\mathbf{S}_v$. The model can be interpreted as a finite deformation analog of the Standard Linear Solid – a spring in parallel with a Maxwell fluid, itself a spring in series with a dashpot.

4.2. Nonlinear viscoelastic model

The nonlinear Sidoroff viscoelastic model of Govindjee and Reese (1997) and Reese and Govindjee (1998a,b) is derived by assuming a multiplicative split of the deformation gradient

$$\mathbf{F} = \mathbf{F}_e \mathbf{F}_v \tag{4.3}$$

into an elastic part $\mathbf{F}_e$ and a viscous part $\mathbf{F}_v$. In addition, we assume that the total free energy is given as a sum of the elastic energy $\Psi_e(\mathbf{C})$ described above and a viscoelastic energy $\Psi_v(\mathbf{C}_e)$ which only depends on the strain associated with the elastic deformation: $\mathbf{C}_e = \mathbf{F}_e^{\top}\mathbf{F}_e$. In the case of isotropy, Ψ_v can also be written as depending on the elastic left Cauchy–Green tensor $\mathbf{b}_e = \mathbf{F}_e\mathbf{F}_e^{\top}$, which yields a more convenient formulation. We define $\Psi_v(\mathbf{b}_e)$ similarly to Ψ_e:

$$\Psi_v = v\Big(\frac{\kappa}{4}(I_3^e - \log I_3^e - 1) + \frac{\mu}{2}(1-s)(I_1^e - \log I_3^e - 3)$$
$$+ \frac{\mu}{2}s(I_2^e - 2\log I_3^e - 3)\Big), \tag{4.4}$$

where I_1^e, I_2^e, I_e^e are the invariants of the three-dimensional tensor $\mathbf{b}_{3e} = \begin{bmatrix} \mathbf{b}_e & 0 \\ 0 & 1 \end{bmatrix}$. $\mathbf{P}_v$ is now given by

$$\mathbf{P}_v = 2\frac{\partial \Psi_v}{\partial \mathbf{b}_e}\mathbf{b}_e\mathbf{F}^{-\top} = v\Big(\frac{\kappa}{2}(I_3^e - 1)\mathbf{I} + \mu(1-s)(\mathbf{b}_e - \mathbf{I}) + \mu s(I_1^e \mathbf{b}_e - \mathbf{b}_e^2 - 2\mathbf{I})\Big)\mathbf{F}^{-\top}. \tag{4.5}$$

The model is completed by giving a *nonlinear* evolution equation for $\mathbf{b}_e$:

$$\dot{\mathbf{b}}_e = \boldsymbol{\ell}\mathbf{b}_e + \mathbf{b}_e\boldsymbol{\ell}^{\top} - 2\mathcal{V}(\boldsymbol{\tau}_e)\mathbf{b}_e, \tag{4.6}$$

where

$$\boldsymbol{\ell} = \dot{\mathbf{F}}\mathbf{F}^{-1},$$
$$\boldsymbol{\tau}_e = 2\frac{\partial \Psi_v}{\partial \mathbf{b}_e}\mathbf{b}_e, \tag{4.7}$$
$$\mathcal{V}(\boldsymbol{\tau}_e) = C_1\Big(\boldsymbol{\tau}_e - \frac{1}{2}(\operatorname{tr} \boldsymbol{\tau}_e)\mathbf{I}\Big) + C_2\frac{1}{2}(\operatorname{tr} \boldsymbol{\tau}_e)\mathbf{I}, \quad C_1, C_2 > 0.$$

Quiescent initial condition now correspond to $\mathbf{b}_e(0) = \mathbf{I}$, which is consistent with the elastic part of the deformation gradient being the identity at time zero. As with the Simo-model, this model can also be interpreted as a finite deformation analog of the Standard Linear Solid.

Reese and Govindjee (1998b) have proved that the Clausius–Duhem inequality is satisfied for their nonlinear viscoelastic model:

$$\frac{1}{2}\mathbf{S} : \dot{\mathbf{C}} - \dot{\Psi}_{total} \geqslant 0, \tag{4.8}$$

but noted that it is unknown whether the linear viscoelastic model of Simo (1987) satisfies this inequality for any appropriate free energy function.

4.3. Steady state spinning of a viscoelastic body

We now derive steady spinning conditions for the viscoelastic variables $\mathbf{Q}$ and $\mathbf{b}_e$. Recall that steady spinning motion of an elastic body is given by

$$\phi(X,t) = \phi(\mathbf{R}(t)X, 0),$$
$$\mathbf{v}(X,t) = \mathbf{v}(\mathbf{R}(t)X, 0). \tag{4.9}$$

The same relationship should hold for any scalar, vector, or tensor quantity defined on the deformed configuration; in particular it should hold for the left Cauchy–Green deformation tensor $\mathbf{b} = \mathbf{F}\mathbf{F}^\top$. Since $\mathbf{b}_e$ is analogous to $\mathbf{b}$, we require $\mathbf{b}_e$ to satisfy

$$\mathbf{b}_e(X,t) = \mathbf{b}_e(\mathbf{R}X, 0), \tag{4.10}$$

where we omit t in the notation for $\mathbf{R}(t)$ in this section. The relationship for other quantities can be determined by using $\mathbf{F}$ to push them onto the deformed configuration. We compute from (4.9) that $\mathbf{F}$ satisfies

$$\mathbf{F}(X,t) = \mathbf{F}(\mathbf{R}X, 0)\mathbf{R}. \tag{4.11}$$

Using this and the integral definition of $\mathbf{Q}$ in (4.1), we find that $\mathbf{Q}$ satisfies

$$\mathbf{R}\mathbf{Q}(X,t)\mathbf{R}^\top = \mathbf{Q}(\mathbf{R}X, 0). \tag{4.12}$$

We then define the transformed variables

$$\widetilde{\mathbf{Q}}(\widetilde{X},t) = \mathbf{R}\mathbf{Q}(X,t)\mathbf{R}^\top,$$
$$\widetilde{\mathbf{b}}_e(\widetilde{X},t) = \mathbf{b}_e(X,t). \tag{4.13}$$

A computation shows that they evolve as

$$\dot{\widetilde{\mathbf{Q}}} = -\frac{1}{\tau}\widetilde{\mathbf{Q}}(t) + \dot{\widetilde{\mathbf{S}}}_e(t) + \mathbf{\Omega}\widetilde{\mathbf{Q}} - \widetilde{\mathbf{Q}}\mathbf{\Omega} - \widetilde{D}\widetilde{\mathbf{Q}}\mathbf{\Omega}\widetilde{X},$$
$$\dot{\widetilde{\mathbf{b}}}_e = \widetilde{\boldsymbol{\ell}}\widetilde{\mathbf{b}}_e + \widetilde{\mathbf{b}}_e\widetilde{\boldsymbol{\ell}}^\top - 2\mathcal{V}(\widetilde{\boldsymbol{\tau}}_e)\widetilde{\mathbf{b}}_e - \widetilde{D}\widetilde{\mathbf{b}}_e\mathbf{\Omega}\widetilde{X}, \tag{4.14}$$

where $\dot{\widetilde{\mathbf{S}}}_e(\widetilde{X},t) = \mathbf{R}\dot{\mathbf{S}}_e(X,t)\mathbf{R}^\top$ may be computed via

$$\dot{\widetilde{\mathbf{S}}}_e = \dot{\widetilde{\mathbf{S}}}_e - \mathbf{\Omega}\widetilde{\mathbf{S}}_e + \widetilde{\mathbf{S}}_e\mathbf{\Omega} + \widetilde{D}\widetilde{\mathbf{S}}_e\mathbf{\Omega}\widetilde{X}.$$

See Potter (2013, Section 3.3) for more details. Again, we now drop the superposed tildes and will only refer to the transformed variables below, with $\dot{\mathbf{S}}_e$ referring to $\dot{\widetilde{\mathbf{S}}}_e$. The weak formulations of the equations of motion for ϕ and $\mathbf{v}$ become

$$\int_{\mathcal{B}} \dot{\phi} \cdot \zeta = \int_{\mathcal{B}} (\mathbf{v} - \mathbf{F}\mathbf{\Omega}X) \cdot \zeta,$$
$$\int_{\mathcal{B}} \dot{\mathbf{v}} \cdot \eta = \int_{\mathcal{B}} -\frac{1}{\rho_R}\mathbf{P}_{total} : D\eta - D\mathbf{v}\mathbf{\Omega}X \cdot \eta. \tag{4.15}$$

The only difference from (2.17) is that $\mathbf{P}_e$ is replaced with $\mathbf{P}_{total}$. This is then coupled with either the linear viscoelastic model

$$\int_{\mathcal{B}} \dot{\mathbf{Q}} : K = \int_{\mathcal{B}} \left(-\frac{1}{\tau}\mathbf{Q}(t) + \dot{\mathbf{S}}_e(t) + \mathbf{\Omega}\mathbf{Q} - \mathbf{Q}\mathbf{\Omega} - D\mathbf{Q}\mathbf{\Omega}X \right) : K \tag{4.16}$$

or the nonlinear viscoelastic model

$$\int_{\mathcal{B}} \dot{\mathbf{b}}_e : K = \int_{\mathcal{B}} (\boldsymbol{\ell}\mathbf{b}_e + \mathbf{b}_e\boldsymbol{\ell}^\top - 2\mathcal{V}(\boldsymbol{\tau}_e)\mathbf{b}_e - D\mathbf{b}_e\mathbf{\Omega}X) : K. \tag{4.17}$$

Here K is an arbitrary symmetric tensor-valued test function in H^1, $\dot{\mathbf{Q}}$ and $\dot{\mathbf{b}}_e$ are in the dual of this space, and $\mathbf{Q}$ and $\mathbf{b}_e$ are symmetric tensor-valued L^2 functions. The convective terms could be integrated by parts to transfer the derivative to K, however we implement it in the code as written. As before, a rigorous well-posedness theory in these spaces is lacking, but the projected dynamics on finite element spaces is well-defined. For later use, we define $\hat{\mathcal{G}}_{vq}$, $\hat{\mathcal{G}}_{vb}$ to be the discretized differential operators corresponding to the linear, Simo, and nonlinear, Sidoroff, viscoelastic models, respectively. We will write $\mathbf{z}^{vq}$ for the triple $(\phi, \mathbf{v}, \mathbf{Q})$ and $\mathbf{z}^{vb}$ for $(\phi, \mathbf{v}, \mathbf{b}_e)$.

The structure of $\hat{\mathcal{G}}_{vb}$ is similar in form to that of LeTallec and Rahier (1994), who also utilized a Sidoroff viscoelastic model in their spinning study. However the structure of $\hat{\mathcal{G}}_{vq}$ differs from other rolling studies that use convolution based models (Oden and Lin, 1986; Faria et al., 1992; Govindjee and Mihalic, 1998). In particular, we treat $\mathbf{Q}$ as an independent field variable. While this increases the number of global unknowns, it avoids well-known issues associated with the accurate computation of $\mathbf{Q}$ at the Gauss points in a finite element computation as well as with the accurate computation of $D\hat{\mathcal{G}}_{vq}$; see for example Govindjee and Mihalic (1998) and Nasdala et al. (1998).

5. Perturbations of the viscoelastic models

We repeat the experiments of Section 3 with the viscoelastic models. The numerical framework changes very little. We model the viscoelastic variables using the same finite element framework and apply Newton's method to solve $\hat{\mathcal{G}}_{vq} = \mathbf{0}$ or $\hat{\mathcal{G}}_{vb} = \mathbf{0}$ to obtain a stationary solution. This involves determining the steady-state values of $\mathbf{Q}$ or $\mathbf{b}_e$ in addition to ϕ and $\mathbf{v}$. In some contexts, notably for incompressible problems involving pressure as a Lagrange multi-
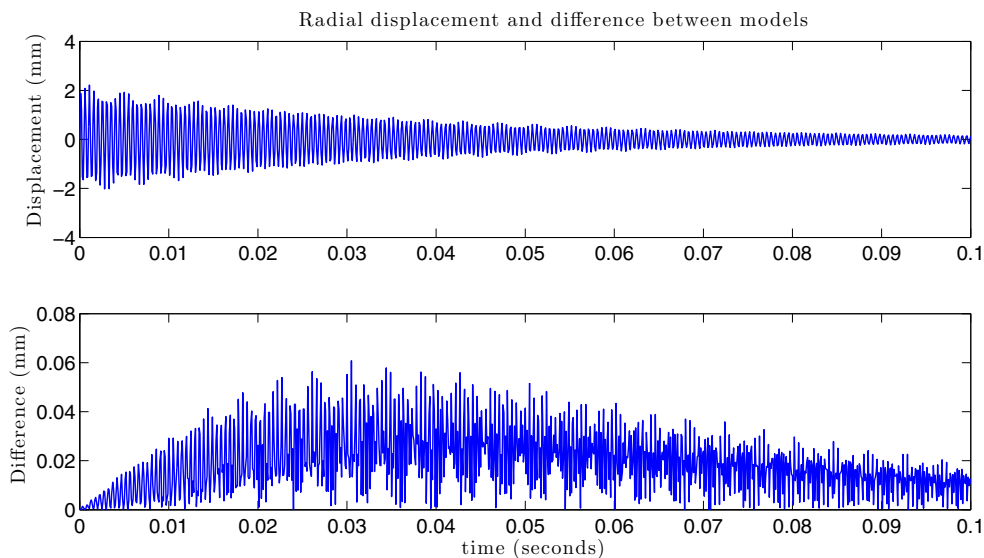

Fig. 10. The top plot shows the radial displacement on the edge of the body for an expanding initial state for the two viscoelasticity models. The bottom plot shows the difference between the models, which is several orders of magnitude smaller than the displacement. As a result, only a single curve can be seen in the top panel.
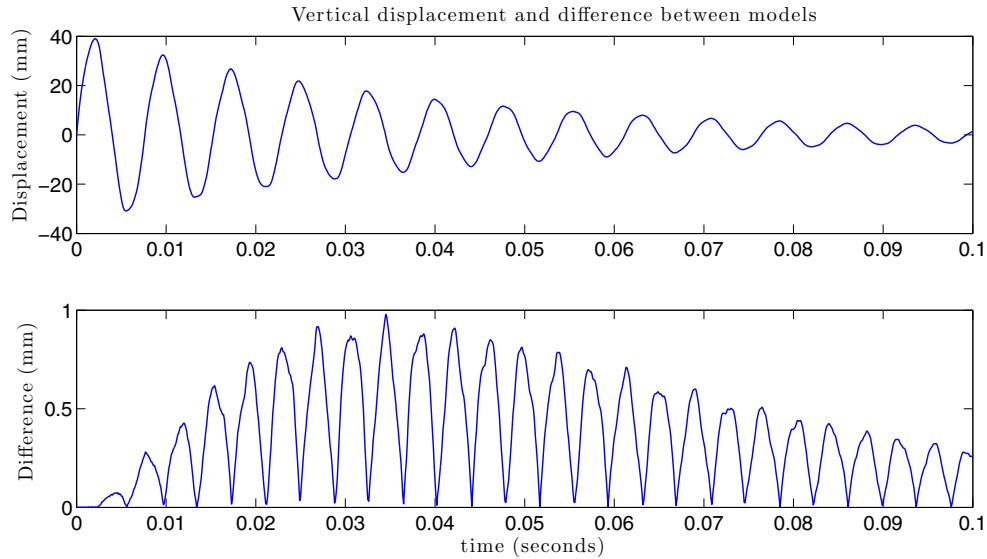
Fig. 11. The top plot shows the vertical displacements on the rightmost edge of the body for a twisting initial state. The bottom plot shows the difference between the models. This difference is small enough that only a single curve can be seen in the top plot.

plier, lower order elements must be used for variables possessing fewer derivatives. However, $\mathbf{Q}$ and $\mathbf{b}_e$ are dynamic variables with time-derivatives explicitly given in the equations of motion, so we do not expect inf–sup type restrictions on the choice of elements. In practice, we do not encounter numerical difficulties using quartic elements for all variables.

The values of the viscoelastic parameters are taken to be $v = 1$ and $\tau = 0.01$ seconds. We choose the constants C_1 and C_2 to be $1/(2\kappa\tau)$ and $1/(2\mu\tau)$, respectively, in order to match the relaxation responses of the Simo and Sidoroff viscoelastic models at small to modest deformations. To illustrate the quality of the match obtained with our parameter selection heuristics, in Figs. 10 and 11 we compare the models' transient relaxation response to initial conditions that excite compression and shear modes, respectively. These initial conditions both have zero initial deformation and quiescent viscoelastic variables, but have an initial velocity that is zero on the hub and increases as one moves away from the hub. For the shear case we specify a clockwise velocity and in the compression case we specify an outward velocity. The differences in the relaxation behavior are seen to be quite minor. Thus, superficially, both models are Standard Linear Solid models with similar short and long time stiffnesses as well as relaxation times.

5.1. Results: steady viscoelastic spinning

We begin by considering the linear viscoelastic model – the Simo model. As with the elastic case, we find a single radially symmetric solution $\mathbf{z}_\omega^{vq}$ for any body speed ω. We compute the eigenvalues of the operator $\hat{\mathcal{G}}_{vq}[\mathbf{z}_\omega^{vq}]$, which we plot in Fig. 12.

A major difference between the eigenvalues in the elastic case (as in Fig. 3), is that the Hamiltonian structure is destroyed and we no longer expect purely imaginary eigenvalues. In fact, all of the eigenvalues we observe have a real component. Moreover, there were no eigenvalues passing through 0, and the matrix $\hat{\mathcal{G}}_{vq}[\mathbf{z}_\omega^{vq}]$ always remains non-singular. Thus we find no bifurcation speeds that lead to other steady state solutions. Yet there is still an event analogous to the critical bifurcation speed ω_c where the imaginary parts of many eigenvalues approach 0, causing them to replace pure decay modes (with zero imaginary part) in the list of the 10 smallest eigenvalues. We will call this speed ω_c^{vq}, which is approximately 285 rad/s.

We plot a set of the smallest magnitude eigenvalues in Fig. 13, and obtain a very similar picture to Fig. 4, with the addition of a real component. We observe that there are eigenvalues of $\hat{\mathcal{G}}_{vq}[\mathbf{z}_\omega^{vq}]$ which have a structure analogous to the λ_i of the elastic case. We will denote these eigenvalues $\lambda_i^{vq}(\omega)$. By "analogous", we mean that the imaginary parts of the λ_i^{vq} form Xs and the corresponding eigenfunction, denoted $\mathbf{e}_i^{vq}$, has a similar structure to the $\mathbf{e}_i$. We will call ω_i^{vq} the speed at which $\text{Im}\{\lambda_i^{vq}(\omega)\} = 0$. However, the ω_i^{vq} are not bifurcation speeds, since the λ_i^{vq} have a non-zero real component. We will refer to them as pseudo-bifurcation speeds. As in the elastic case of Section 3.3, we also observe eigenvalues $\lambda_{i,j}^{vq}$ and eigenfunctions $\mathbf{e}_{i,j}^{vq}$ that correspond to the second hierarchy of standing waves, i.e. this second hierarchy of eigenfunctions persists in the viscoelastic case.

When we examine the nonlinear viscoelastic model (the Sidoroff model), we see similar results. Specifically, the eigenvalues λ_i^{vb} (with corresponding eigenfunctions denoted $\mathbf{e}_i^{vb}$) have a real component; $\hat{\mathcal{G}}_{vb}$ remains non-singular; there is critical speed ω_c^{vb} (near 290 rad/s); and the eigenfunctions outside of Oden and Lin's i-peak hierarchy remain. Fig. 14 shows the trajectories of the λ_i^{vb} when ω is varied. Notice, however, that there is one major difference between the linear and nonlinear models: the real parts of the λ_i^{vq} steadily increase as ω increases while the real parts of the λ_i^{vb} remain level (see Figs. 13 and 14). We investigate this crucial difference in the next section.

6. Stability of the viscoelastic models

For large enough ω we observe from Fig. 13 that λ_3^{vq} has a positive real part, which indicates an unstable mode of the stationary solution for the linear viscoelastic model. To examine further, we perturb the stationary solution corresponding to rotational speed $\omega_3^{vq} \approx 461$ rad/s in the direction $\text{Re}\{\mathbf{e}_3^{vq}\}$ and allow the body to evolve in time according to the nonlinear dynamics with this initial configuration using a 5th or 8th order Runge–Kutta time-stepping scheme (Dormand and Prince, 1989; Hairer et al., 2000). The cost of quartic finite elements and high-order Runge–Kutta methods is compensated by larger stability regions and higher accuracy per gridpoint and timestep. Choosing the real part of the eigenvector for the perturbation keeps the calculation real, and boils down to selecting an arbitrary phase in the oscillatory part of the linearized
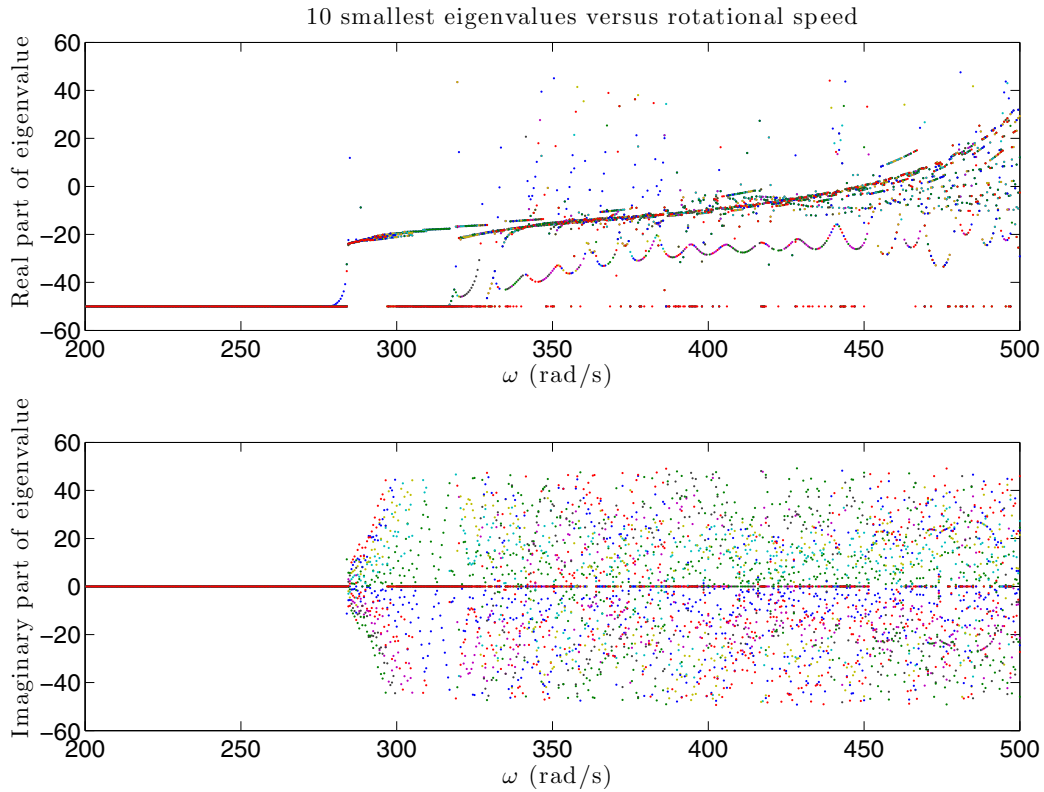
Fig. 12. (Simo-class model) Plots of the smallest eigenvalues of $\hat{\mathcal{G}}_{vq}[\mathbf{z}_\omega^{vq}]$. Here ω_c^{vq} is near 285 rad/s.
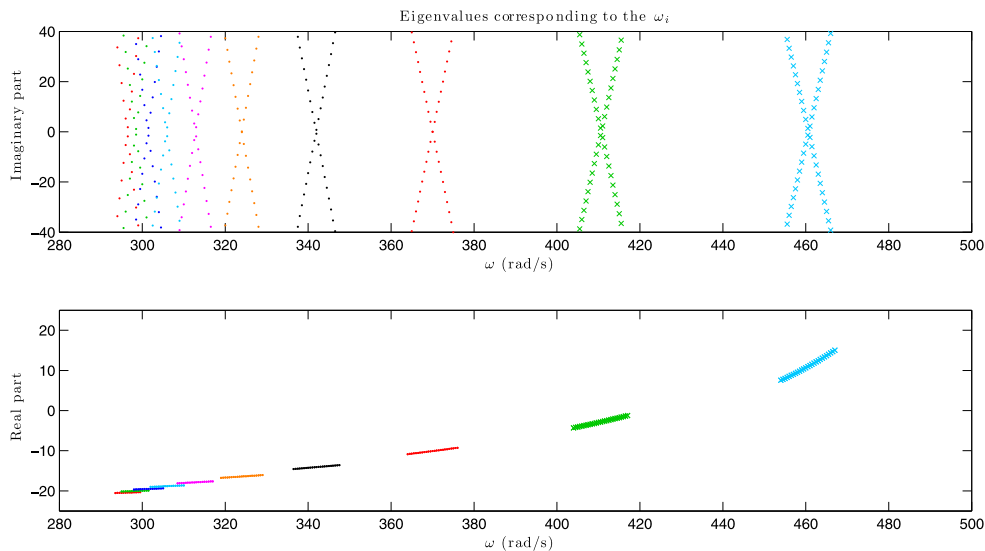

Fig. 13. (Simo-class model) Real and imaginary components of the λ_i^{vq}. The leftmost X corresponds to λ_{12}^{vq} while the rightmost X corresponds to λ_3^{vq}.

solution associated with the unstable eigenvalue. The idea is to seed the nonlinear evolution with an unstable linearized mode, so the phase is unimportant. Counter to the common intuition surrounding viscoelastic response, we observe that the system exponentially gains energy to the point that our numerical time-stepper returned NaNs. We observe the same phenomenon with any initial condition evolved at rotation speeds greater than approximately 420 rad/s.

Fig. 15 shows the exponential increase in elastic energy with time. To ensure that this non-physical behavior of the linear visco-

elastic model was not caused by any numerical issues, Fig. 15 shows the energy versus time curves for several mesh sizes and for two different time-step sizes. The results indicate that the model response has been fully resolved and, thus, that the instability is intrinsic to the model. We also repeated the experiment with the elastic model and nonlinear viscoelastic models using analogous initial conditions: $\mathbf{z}_\omega$ was perturbed in the direction Re$\{\mathbf{e}_3\}$ with speed $\omega = 470$ rad/s $\approx \omega_3$ for the elastic model and $\mathbf{z}_\omega^{vb}$ was perturbed in the direction Re$\{\mathbf{e}_3^{vb}\}$ with speed $\omega = 547$ rad/s $\approx \omega_3^{vb}$ for the nonlinear viscoelastic model. Figs. 16 and 17 show
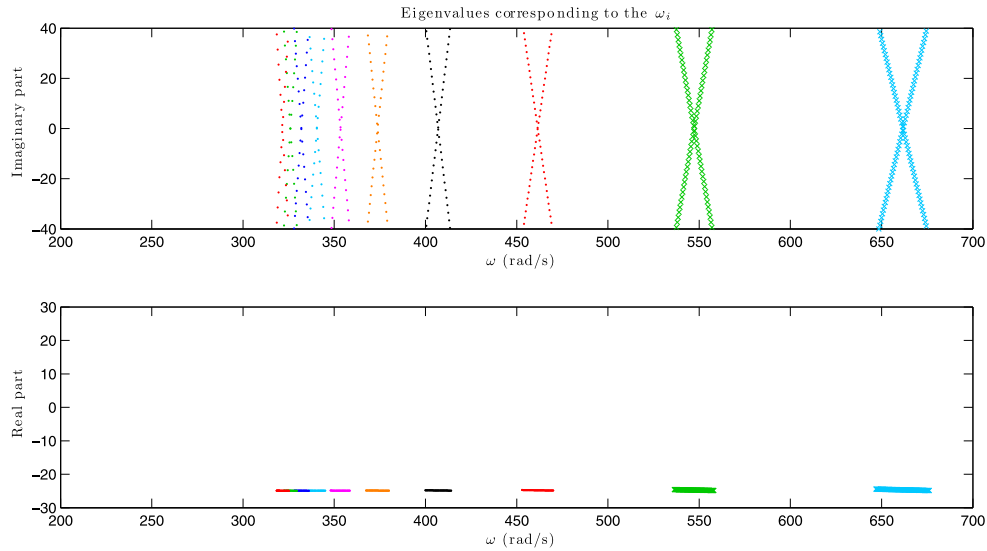
Fig. 14. (Sidoroff-class model) Real and imaginary components of the λ_i^{vb}. The leftmost X corresponds to λ_{12}^{vb} while the rightmost X corresponds to λ_3^{vb}.
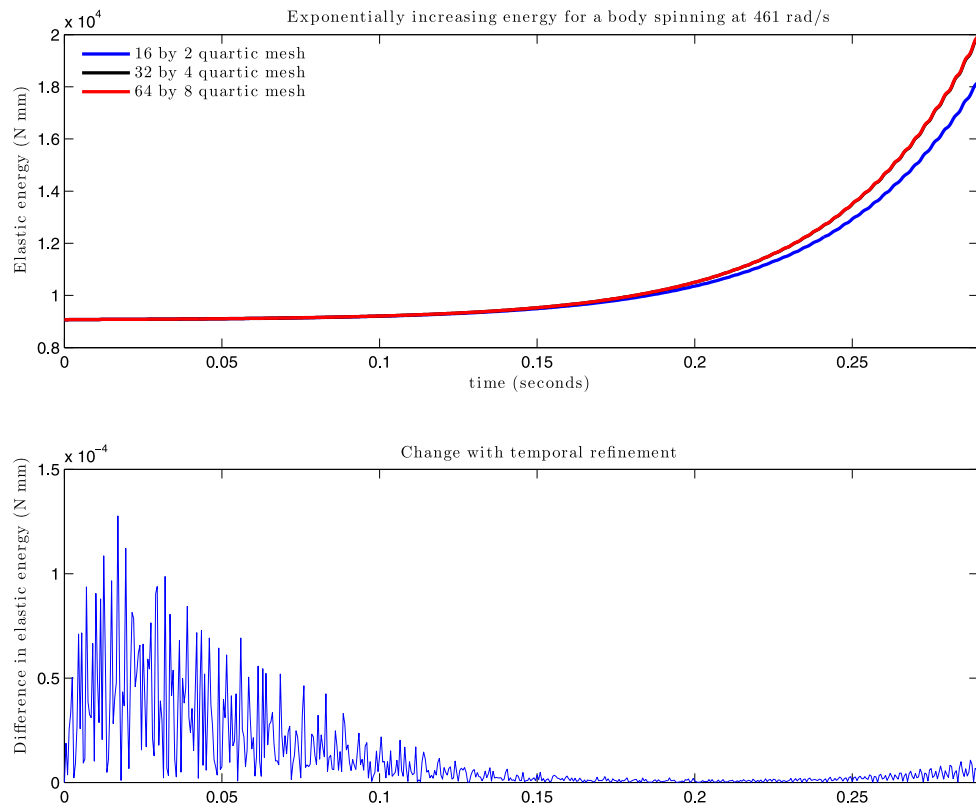

Fig. 15. The upper plot shows the elastic energy for the steady state solution of the Simo-class viscoelastic model perturbed in the direction of Re$\{\mathbf{e}_3^{vq}\}$. We repeat the calculation for three mesh sizes. The discrepancy between the finer meshes is barely visible on the plot. The lower plot shows the difference when halving the time step for the finest mesh; note the scale.

the results of these experiments. In contrast to the linear viscoelastic model, the simulations show no exponential increase of the energy or other signs of instability. These results provide strong evidence that it is the linear viscoelastic model itself that causes the non-physical exponential increase in energy. For a large range of viscoelastic parameters, we observed blow up in the linear Simo-model, but never in the nonlinear Sidoroff-model. For the same range of parameters we also always observed that the real part of the λ_i^{vq} increases nearly linearly with the rotational speed

(see Fig. 13), which suggests that no matter what parameters we choose, the $\mathbf{e}_i^{vq}$ become unstable at high enough rotational speeds. In contrast, if we look closely at the λ_i^{vb}, we see that their real parts decrease as ω increases, suggesting that the $\mathbf{e}_i^{vb}$ always remain stable; see Fig. 18.

The instability of the linear viscoelastic Simo-model is perhaps not surprising considering that the evolution operator is linear in the viscoelastic variables but is applied in a finite deformation setting. It is expected to work well for small deformations, but not so
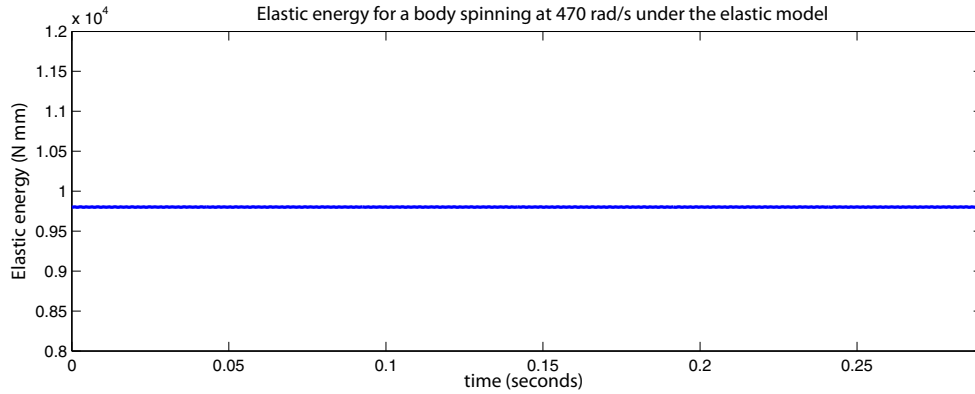
Fig. 16. Elastic energy for the steady-state solution of the elastic model perturbed in the direction of Re{$\mathbf{e}_3$}. Unlike the Simo-class viscoelastic case, the elastic energy does not increase.
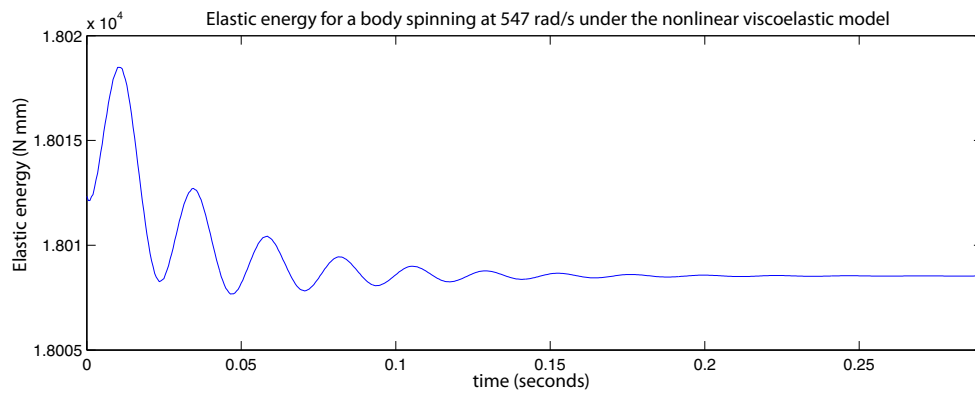

Fig. 17. Elastic energy for the analogous spinning initial condition as in Fig. 15, but using the Sidoroff-class model of viscoelasticity perturbed in the direction Re{$\mathbf{e}_3^{vb}$}. Unlike the Simo-class viscoelastic model case, the elastic energy does not increase, on average.
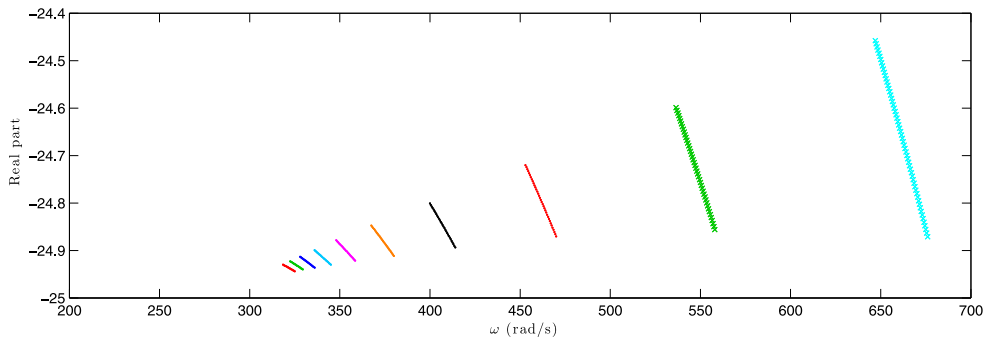

Fig. 18. (Sidoroff-class model) Real components of the λ_i^{vb}.

when large deformations cause nonlinear effects to become important. This is exactly what we observe: at small rotation speeds, when there is less deformation, the linear viscoelastic model behaves as one expects, i.e. in a dissipative manner. However, at high rotation speeds and large deformations the linear viscoelastic model behaves non-physically. The nonlinear viscoelastic Sidoroff-model does not suffer from these problems since it properly takes into account large deformations while explicitly satisfying the Clausius–Duhem inequality.

7. Conclusions

We have presented a formulation of the axisymmetric spinning body suitable for both steady as well as transient behavior. In the hyperelastic steady setting, we have elucidated a more complex hierarchy of bifurcation modes than have been discussed in the literature to date. This was achieved by a careful examination of the smallest magnitude eigenvalues of the linearized evolution operator. This same formulation was also extended to the finite deformation viscoelastic setting. In this setting we have identified pseudo-bifurcation modes that can be associated to a discrete set of critical frequencies. By perturbing the system from an axisymmetric state in the direction of a linearly unstable pseudo-bifurcation mode and then (nonlinearly) following the system in time, we have been able to show that the Simo-class of models for (linear) finite viscoelasticity lead to exponential growth in elastic energy in time. Thus such models are seen to be unstable, counter to intuition about convolution type models with fading memory. On the

other hand, a similar analysis using a (purely) hyperelastic model is fully stable, as is a similar analysis using a Sidoroff-class model, which is necessarily thermodynamically stable. This points to the general conclusion that it is not prudent to utilize linear finite viscoelastic models of the Simo-class. In particular, in tire analyses in which a steady spinning state is perturbed to obtain a transient evolution, non-physical unstable computations are clearly possible. This undesirable situation can be rectified by using nonlinear finite viscoelastic models that provably satisfy the second law of thermodynamics.

Acknowledgments

References

Ball, J.M., 1977. Convexity conditions and existence theorems in nonlinear elasticity. Arch. Ration. Mech. Anal. 63, 337–403.

Bass, J.M., 1987. Three-dimensional finite deformation, rolling contact of a hyperelastic cylinder: formulation of the problem and computational results. Comput. Struct. 26, 991–1004.

Bernstein, B., Kearsley, E.A., Zapas, L.J., 1963. A study of stress relaxation with finite strains. Trans. Soc. Rheol., 391–410.

Cai, Z., Manteuffel, T.A., McCormick, S.F., 1997a. First-order system least squares for the Stokes equations, with application to linear elasticity. SIAM J. Numer. Anal. 34 (5), 1727–1741.

Cai, Z., Manteuffel, T.A., McCormick, S.F., 1997b. First-order system least squares for second-order partial differential equations: Part II. SIAM J. Numer. Anal. 34 (2), 425–454.

Chatterjee, A., Cusumano, J.P., Zolock, J.D., 1999. On contact-induced standing waves in rotating tires: experiment and theory. J. Sound Vib. 227, 1049–1081.

Ciarlet, P.G., 1988. Mathematical Elasticity. North-Holland, Amsterdam.

Coleman, B.D., 1964a. On thermodynamics, strain impulses, and viscoelasticity. Arch. Ration. Mech. Anal. 17, 230–254.

Coleman, B.D., 1964b. Thermodynamics of materials with memory. Arch. Ration. Mech. Anal. 17, 1–46.

Coleman, B.D., Noll, W., 1963. The thermodynamics of elastic materials with heat conduction and viscosity. Arch. Ration. Mech. Anal. 13, 167–178.

Dormand, J.R., Prince, P.J., 1989. Practical Runge–Kutta processes. SIAM J. Sci. Stat. Comput. 10, 977–989.

Evans, L.C., 1998. Partial differential equations. Graduate Studies in Mathematics, vol. 19. American Mathematical Society, Providence, RI.

Faria, L.O., Oden, J.T., Yavari, B., Tworzydlo, W.W., Bass, J.M., Becker, E.B., 1992. Tire modeling by finite elements. Tire Sci. Technol. 20, 33–56.

Govindjee, S., Reese, S., 1997. A presentation and comparison of two large deformation viscoelastic models. ASME J. Eng. Mater. Technol. 119, 251–255.

Govindjee, S., Mihalic, P.A., 1998. Viscoelastic constitutive relations for the steady spinning of a cylinder. Tech. Report UCB/SEMM-98/02, University of California Berkeley, Department of Civil Engineering.

Hairer, E., Norsett, S.P., Wanner, G., 2000. Solving ordinary differential equations I: Nonstiff problems, second ed. Springer, Berlin.

Hughes, T.J.R., Kato, T., Marsden, J.E., 1977. Well-posed quasi-linear second-order hyperbolic systems with applications to nonlinear elastodynamics and general relativity. Arch. Ration. Mech. Anal. 63 (3), 273–294.

Iooss, G., Plotnikov, P.I., Toland, J.F., 2005. Standing waves on an infinitely deep perfect fluid under gravity. Arch. Ration. Mech. Anal. 177, 367–478.

Kennedy, R., Padovan, J., 1987. Finite element analysis of steady and transiently moving/rolling nonlinear viscoelastic structure – II. Shell and three-dimensional simulations. Comput. Struct. 27, 249–257.

Lehoucq, R.B., Sorensen, D.C., Yang, C., 1998. ARPACK Users' Guide: Solution of Large-Scale Eigenvalue Problems with Implicitly Restarted Arnoldi Methods, vol. 6. SIAM.

LeTallec, P., Rahier, C., 1994. Numerical models of steady rolling for non-linear viscoelastic structures in finite deformations. Int. J. Numer. Methods Eng. 37, 1159–1186.

Li, X.S., Demmel, J.W., 2003. SuperLU DIST: A scalable distributed-memory sparse direct solver for unsymmetric linear systems. ACM Trans. Math. Software (TOMS) 29, 110–140.

Marsden, J., Hughes, T.J.R., 1983. Mathematical Foundations of Elasticity. Prentice-Hall Inc., Englewood Cliffs, NJ.

Nasdala, L., Kaliske, M., Becker, A., Rothert, H., 1998. An efficient viscoelastic formulation for steady-state rolling structures. Comput. Mech. 22, 395–403.

Oden, J.T., Lin, R., 1986. On the general rolling contact problem for finite deformations of a viscoelastic cylinder. Comput. Methods Appl. Mech. Eng. 57, 297–367.

Padovan, J., 1987. Finite element analysis of steady and transiently moving/rolling nonlinear viscoelastic structure – I. Theory. Comput. Struct. 27, 249–257.

Padovan, J., Paramodilok, O., 1983. Generalized solution of time dependent traveling load problem via moving finite element scheme. J. Sound Vib. 91, 195–209.

Padovan, J., Paramodilok, O., 1985. Transient and steady state viscoelastic rolling contact. Comput. Struct. 20, 545–553.

Potter, T., 2013. Dynamics and Stability of Rolling Viscoelastic Tires (Ph.D. thesis). University of California, Berkeley.

Rabier, P.J., Oden, J.T., 1989. Bifurcation in rotating bodies. Recherches en Mathématiques Appliquées. Masson, Paris.

Reese, S., Govindjee, S., 1998a. Theoretical and numerical aspects in the thermo-viscoelastic material behaviour of rubber-like polymers. Mech. Time-Depend. Mater. 1, 357–396.

Reese, S., Govindjee, S., 1998b. A theory of finite viscoelasticity and numerical aspects. Int. J. Solids Struct. 35, 3455–3482.

Russel, J.S., 1845. Report on waves. In: Report of the fourteenth meeting of the British Association for the Advancement of Science, London, pp. 311–390.

Rycroft, C.H., Wilkening, J., 2013. Computation of three-dimensional standing water waves. J. Comput. Phys. 255, 612–638.

Sidoroff, F., 1974. Un modèle viscoélastique non linéaire avec configuration intermédiaire. J. Méc. 13, 679–713.

Simo, J.C., 1987. On a fully three-dimensional finite-strain viscoelastic damage model: formulation and computational aspects. Comput. Methods Appl. Mech. Eng. 60, 153–173.

Truesdell, C., Noll, W., 1965. The Non-Linear Field Theories of Mechanics. Springer-Verlag, Berlin.

Wilkening, J., 2011. Breakdown of self-similarity at the crests of large amplitude standing water waves. Phys. Rev. Lett. 107, 184501.

Wilkening, J., Yu, J., 2012. Overdetermined shooting methods for computing standing water waves with spectral accuracy. Comput. Sci. Disc. 5, 014017.